Enhanced Cycling Performance of Ni-Rich Positive Electrodes (NMC) in Li-Ion Batteries by Reducing Electrolyte Free-Solvent Activity

Citation: Tatara, Ryoichi et al. "Enhanced Cycling Performance of Ni-Rich Positive Electrodes (NMC) in Li-Ion Batteries by Reducing Electrolyte Free-Solvent Activity." ACS Applied Materials and Interfaces 11, 38 (July 2019): 34973–34988 © 2019 American Chemical Society

As Published: http://dx.doi.org/10.1021/acsami.9b11942

Publisher: American Chemical Society (ACS)

Persistent URL: https://hdl.handle.net/1721.1/128703

Version: Author's final manuscript: final author's manuscript post peer review, without publisher's formatting or copy editing

ACS Applied Materials & Interfaces

Enhanced Cycling Performance of Ni-rich Positive Electrodes (NMC) in Li-ion Batteries by Reducing Electrolyte Free-solvent Activity

Ryoichi Tatara†‡*[a], Yang Yu†[b], Pinar Karayaylali†[c], Averey K. Chan[b,d], Yirui Zhang[c], Roland Jung[e], Filippo Maglia[e], Livia Giordano[a, c], Yang Shao-Horn*[abc]

[a] Research Laboratory of Electronics, [b] Department of Material Science and Engineering, [c] Department of Mechanical Engineering, Massachusetts Institute of Technology, 77 Massachusetts Ave., Cambridge, MA 02139, United States

[d] Department of Materials, Imperial College London, Royal School of Mines Building, Prince Consort Rd., London, SW7 2AZ, UK

[e] BMW Group, Petuelring 130, 80788 Munich, Germany

† Contributed equally

‡ Present address: Department of Chemistry and Biotechnology, Yokohama National University, 79-5 Tokiwadai, Hodogaya-ku, Yokohama, Kanagawa, 240-8501, Japan

* Corresponding authors (shaohorn@mit.edu, tatara-ryoichi-nx@ynu.ac.jp)

Key words: Concentrated Electrolyte, Activity, Solvation Structure, Li-ion Batteries, Electrode-electrolyte Interface, Ni-rich Positive Electrodes, NMC

Abstract

The interfacial (electro-)chemical reactions between electrode and electrolyte dictate the cycling stability of Li-ion batteries. Previous experimental and computational results have shown that replacing Mn and Co with Ni in layered $LiNi_xMn_yCo_{1-x-y}O_2$ (NMC) positive electrodes promotes the dehydrogenation of carbonate-based electrolytes on the oxide surface, which generates protic species to decompose $LiPF_6$ in the electrolyte. In this study, we utilized this understanding to stabilize $LiNi_{0.8}Mn_{0.1}Co_{0.1}O_2$ (NMC811) by decreasing free-solvent activity in the electrolyte through controlling salt concentration and salt dissociativity. Infrared spectroscopy revealed that highly concentrated electrolytes with low free-solvent activity had no dehydrogenation of ethylene carbonate, which could be attributed to slow kinetics of dissociative adsorption of Li^+-coordinated solvents on oxide surfaces. The increased stability of the concentrated electrolyte against solvent dehydrogenation gave rise to high capacity retention of NMC811 with capacities greater than 150 $mAhg^{-1}$ (77 % retention) after 500 cycles without oxide-coating, Ni-concentration gradients, or electrolyte additives.

1. Introduction

$LiNi_xMn_yCo_zO_2$ (NMC) are promising positive electrode materials in high-energy Li-ion batteries for electric vehicle applications.[1–5] Understanding and controlling the (electro-) chemical reactions at the interface between NMC and the electrolyte is the key to enable stable cycling of these high-energy Li-ion batteries.[6–8] Increasing Ni content in the NMC series from $LiNi_{1/3}Mn_{1/3}Co_{1/3}O_2$ (NMC111) to Ni-rich NMC such as $LiNi_{0.6}Mn_{0.2}Co_{0.2}O_2$ (NMC 622) and $LiNi_{0.8}Mn_{0.1}Co_{0.1}O_2$ (NMC811) can greatly increase discharge capacity[1,2,9] but at the expense of capacity loss during cycling,[1,9–11] accompanied by lower voltage onset of O_2 and CO_2 gas evolution.[9,12] Even though

upper voltage limits used to cycle Ni-rich NMC are much lower than the electrochemical oxidation voltage limit (~5 V_{Li}) of conventional electrolytes,[13] which typically consist of 1.0 M $LiPF_6$ dissolved in cyclic carbonates such as ethylene carbonate (EC) and linear carbonates (*e.g.* ethyl methyl carbonate - EMC)[13], greater decomposition of solvent[2,9,14,15] and salt decomposition[14] has been reported for NMC cycling with increased Ni content. The enhanced electrolyte degradation found for Ni-rich oxides[9,12,14] has been attributed to greater reactivity between the electrolyte and charged oxide surfaces[8,14,16,17] and/or singlet-oxygen[9,18] liberated from Ni-rich oxides during charging. Recent density functional theory (DFT) calculations have shown that the thermodynamic driving force for dissociative adsorption of carbonate solvents increases with greater M-O covalency[19–23] by having more later transition metals such as Ni or less lithium in the layered structure, where carbonate solvents including ethylene carbonate (EC) and ethyl methyl carbonate (EMC) dehydrogenate on surface oxygen of Li_xMO_2 to form a surface hydroxyl group (*e.g.* $C_3O_3H_3^+$–$O_{surface}$ and H^+–$O_{surface}$).[16,24,25] This proposed carbonate dehydrogenation is supported by *ex-situ* Fourier transform infrared (FT-IR) and Raman spectroscopy experiments[14] while the protic species generated from carbonate dehydrogenation can further react with $LiPF_6$ to produce less-fluorine coordinated species[14,26,27] including PF_3O and $PF_2O_2^-$ as revealed from X-ray photoelectron spectroscopy (XPS) and nuclear magnetic resonance (NMR) results.[14] This proposed mechanism – oxide-mediated electrolyte oxidation – is in agreement with previous reports that tuning Ni-rich NMC surface through a less-M-O-covalent coating[25,28–32] or creating a Ni-poor protective layer[33–36] can greatly increase capacity retention of Ni-rich NMC electrodes. For example, recent FT-IR measurements have shown that an Al_2O_3-coating on NMC622 can reduce carbonate dehydrogenation and $LiPF_6$ decomposition, which is associated with greater cycling stability than uncoated NMC622.[37] Moreover, altering the electrolyte compositions by including additives[38–43] or increasing salt concentrations[44] can enhance capacity retention of Ni-

rich NMC. Inaba *et al.*[44–49] have shown that increasing $LiBF_4$ concentration in propylene carbonate (PC) to ~3.5 M (7.25 mol/kg), NMC532 can retain a capacity of 185 mAh/g after 50 cycles to 4.6 V_{Li} while that in ~1 M decays to 140 mAh g^{-1}. [45] In addition, by increasing $LiBF_4$ concentration in DMC to ~ 4 M (8.67 mol/kg), NMC811 exhibited a capacity of 190 mAh/g after 50 cycles to 4.3 V_{Li} while that in ~1 M decays to 140 mAh g^{-1}.[44] The change in solvation structure and the proportion of free solvent can affect the electrochemical stability of the solvent. In the presence of Li^+ solvation, DFT calculations[50–53] and molecular dynamics (MD)[50] studies show that the solvent molecule is stabilized by bond formation with Li^+, which stabilizes the solvent's electron lone-pairs, decreasing the electron energy level at the highest occupied molecular orbital (HOMO) states and increasing the oxidative stability of the solvents.[50] The stabilization of the solvent through Li^+ coordination is further supported experimentally by several research groups.[44–47,54–57] However, as mentioned previously, upper voltage limits used to cycle Ni-rich NMC (4.4-4.6 V_{Li})[9,37] are much lower than the simple electrochemical oxidation potential (~5 V_{Li}) of even conventional electrolytes solutions (~1 M).[13] Thus, the physical origin of enhanced stability due to increased salt concentration is still not well understood, which is the focus of this study. In the present manuscript, we propose a new concept, where Li-coordination with carbonates – greatly decreases the kinetics of dehydrogenation supported by DFT than free carbonates, which is responsible for increased capacity retention during cycling of NMC811.

Here we examine this oxide-mediated electrolyte oxidation mechanism[14,16,17,37,58] by employing highly concentrated carbonate-based electrolytes and electrolyte salts of different dissociation constants, and test if having fewer free carbonate molecules can potentially reduce the electrolyte reactivity with Ni-rich NMC. Highly concentrated electrolytes that typically have a salt molar concentration greater than ~3 M and a molar ratio of Li:solvent less than 1:4, have shown radically different properties such as reduced volatility/flammability [55,59–64],

greater electrochemical stability window[65–69], enhanced rate performance[56,68,70–72], and altered interfacial reactivity[61,66–68,70,73–79] from conventional electrolytes (~1 M).[13,80] These changes have been attributed to the reduction of free solvent molecules that do not coordinate with Li ions[62,81–83]. For example, Inaba *et al.* first reported that lithium can be intercalated reversibly into graphite in a concentrated electrolyte of propylene carbonate (PC) in 2003[84] while conventional PC-based electrolytes failed to form a stable SEI with graphite[13]. In addition, Winter and Placke *et al.*, showed that the oxidative stability expanded to ~6 V_{Li} with 4 M $LiPF_6$ in DMC.[85] Moreover, Watanabe *et al.* have reported that the oxidation potential of ether-based electrolytes, having lithium bis(trifluoromethanesulfonyl)imide: LiTFSI with triglyme and tetraglyme, can be increased from ~4.0 V_{Li} in ~0.2 M to ~4.5 V_{Li} in ~3 M by removing free ether solvent molecules (1:1 molar mixture of LiTFSI with glyme), where enhanced stability against oxidation is associated with lower HOMO energy level of Li^+-coordinated solvents.[55]

In this work, to understand the mechanism of improved stability through changing electrolyte solvation structures, we quantify the amounts of free carbonate solvents when increasing $LiPF_6$ salt concentration from 0.2 to 3.1 M and by changing anions from BF_4^-, PF_6^- to $TFSI^-$ with increasing lithium salt dissociation constant[86–88] in 1.0 M electrolytes using Raman spectroscopy. The amounts of free carbonate solvents in 1.0 and 3.1 M were discussed and correlated with capacity loss and impedance growth of NMC811 during cycling with these electrolytes. The dissociativity of the salt in solvent also largely dictates the amount of free Li^+ in the electrolyte as well as the Li^+ coordination of the solvent species. The association strength of different common anions used in lithium-ion battery salts can be ranked as $TFSI^-$~PF_6^-<AsF_6^-<ClO_4^-<BF_4^-,[53,89,90] where $TFSI^-$ and PF_6^- are the most dissociative with more free Li^+ ions when dissolved in a carbonate electrolyte, and BF_4^- is the most associative with more cation-anion pairs

instead of free Li^+. In addition, carbon-free and binder-free oxide-only electrodes charged in these two electrolytes (1 and 3.1 M) to different voltages in the first cycle were analyzed by FT-IR, Raman spectroscopy and XPS to identify oxidized or decomposed products of carbonate and salt, from which the role of free carbonate solvents on the electrolyte reactivity with NMC surface, and implications on the capacity loss and impedance of NMC during cycling are discussed.

2. Methods

2.1 Experimental methods

Materials 1.0 M (mol/L) $LiPF_6$ in a 3:7 wt:wt ethylene carbonate (EC): ethyl methyl carbonate (EMC) (LP57, battery-grade, BASF), $LiPF_6$ (>99.99%, battery-grade, Aldrich), $LiBF_4$ (>99.99%, ultra-dry-grade, Aldrich), EC (battery-grade, BASF), EMC (battery-grade, BASF) were used as received. The electrolytes (except for LP57) were prepared by simple mixing of $LiPF_6$ or $LiBF_4$ and EC or EMC in an Argon-filled glove box (MBraun, < 0.5 ppm of H_2O and O_2). The residual water contents in the electrolytes were measured by Karl Fischer titration and were less than 20 ppm.

Viscosity, density and ionic conductivity The viscosities and densities of the electrolytes were measured by using a Stabinger viscometer (SVM3001, Anton Paar). Ionic conductivity was measured by using the complex impedance method with the conductivity cell (CONPT-BTA, Vernier). The cell constant of the conductivity probe was calculated by measuring the conductivity of a standard solution (0.01 M KCl aqueous solution, 1.413 mS/cm at 25 ºC, VWR). The density, viscosity and ionic conductivity for the concentrations of $LiPF_6$ (0, 0.22, 0.43, 1.0, 1.3, 2.0, 2.4 and 3.1 M) in EC/EMC, and $LiClO_4$ and $LiBF_4$ (1.0 M) in EC/EMC solutions at 25 ºC were measured, where details are shown in **Table S1 and Table**

S2, respectively. In addition, the viscosity, density and ionic conductivity of 1.5 and 1.0 M $LiPF_6$ solution in pure EC or EMC at 25 °C are shown for comparison in **Table S3**, where the viscosity and density of EC was measured at a supercooled liquid state at 25 °C as the melting point of EC is ~35 °C. Moreover, activation energy was calculated from temperature dependent data of viscosity and ionic conductivity measurements, where the plots were fitted only for the high-temperature region (**Figure S1**).

Oxide synthesis and electrode preparation NMC111 ($LiNi_{0.33}Mn_{0.33}Co_{0.33}O_2$) was prepared as reported previously.[14] NMC622 and NMC811 were obtained from ECOPRO, South Korea. Both NMC622 and NMC811 had no-coating and no-Ni concentration gradient within individual oxide particles, which was used to examine the intrinsic stability/reactivity trend of the electrode-electrolyte interface.

The carbon-free and binder-free pellet electrodes were prepared as reported previously.[14] The pellet electrodes were used for DRIFT and Raman measurements. The carbon-free binder-free oxide powder electrodes were also prepared as reported previously.[14] The carbon-free, binder-free powder electrodes were used for XPS measurements. The active material loading was ~2.4 mg/cm^2.

The composite positive electrodes for battery cycling and EIS measurements were composed of 85 wt% of NMC811 as an active material, carbon black (5 wt % KS6 and 2 wt% Super P, both from Timcal) as an electrically conductive additive, and poly(vinylidene fluoride) (8 wt%, PVDF, Kynar) as a polymer binder. The mesh reference electrode was also composed of 80 wt% of $Li_4Ti_5O_{12}$ (LTO, Itasco, >99.5 %), 10 wt% of acetylene black (C-55, Chevron) and 10 wt% of PVDF. Detail electrode preparation method can be found in previous report.[58] Each electrode was punched with a 1/2 inch diameter (1.27 cm diameter) for NMC811

(on Al foil) and 18 mm diameter for $Li_4Ti_5O_{12}$ mesh reference. The active material loading was ~2.4 mg/cm^2 for composite electrodes and ~1 mg/cm^2 for $Li_4Ti_5O_{12}$ mesh reference electrodes, respectively. After compression at 6.3 T/cm^2, the thickness of NMC811 composite electrodes was ca. 10 μm, packing density was ca. 3.2 $g_{NMC\text{-}C\text{-}PVDF}$/cm^3 and porosity was ~18 %. Particle size and specific surface area of NMC811 used in this work is d = 5-10 μm and 0.334 m^2/g, respectively.

Electrochemical measurements Electrochemical behavior of the carbon-free, binder-free electrodes and pellet electrodes were confirmed by galvanostatic measurements in two-electrode cells (Tomcell type TJ-AC, disk type two-electrode cell). Cells were assembled in an argon-filled glovebox (MBraun, <0.5 ppm of H_2O and O_2) and comprised a lithium metal foil negative electrode (15 mm diameter) and the positive electrode (1/2 inch (12.7 mm) diameter), separated by two pieces of polyolefin separator (Celgard 2325, 21 mm diameter) or a piece of glass fiber separator (Whatman GF/A, Aldrich, 21 mm diameter, dried at 150 ^{o}C in vacuum for overnight prior to use, glass fiber separator was used for concentrated electrolyte, 3.1 M $LiPF_6$ in EC/EMC solution, due to issues with wettability for polyolefin separators), with 100 μL of different electrolytes. The cells were charged with different end-of-charge potentials (4.1, 4.2, 4.4, 4.6 and 4.8 V_{Li}) at a C/100 rate and held at the potential for 5 hours at room temperature with VMP3 potentiostat (Biologic), based on the theoretical capacity calculated assuming full delithiation ($LiNi_xMn_yCo_{1-x-y}O_2 \rightarrow Li^+ + e^- + Ni_xMn_yCo_{1-x-y}O_2$, ~275 mAh g^{-1}, 1C = 275 mA g^{-1}).

For electrochemical impedance spectroscopy (EIS) and battery cycling experiments with composite electrodes, three-electrode cells were assembled in an argon-filled glove box

with Li metal foil (15 mm diameter), $Li_4Ti_5O_{12}$ mesh reference electrode (18 mm diamter), and NMC811 composite electrode (1/2 inch (12.7 mm) diameter) with Whatman GF/A separators (19 mm diameter). A mesh reference electrode was used to avoid an artefactual EIS response.[58,91,92] A detailed cell configuration can be found in the previous work.[58] NMC811 working electrodes were then charged at 27.5 mA/g (C/10 rate, 27.5 mA/g corresponds to ~65 $\mu A/cm^2$ for average loading density of ~2.4 mg/cm^2) and held at potentials of 3.9, 4.0, 4.1, 4.2, 4.3, 4.4, 4.5 and 4.6 V_{Li} for 1 hour, and relaxed for 1 hour. After each relaxation, EIS measurements were carried out at the open circuit potential with 10 mV amplitude and frequency range from ~10^{-2} to 10^6 Hz. In this work, due to high R_{HF} on NMC811 electrodes (at some conditions it cannot even form a complete semicircle within this frequency range, down to 100 mHz) and overlapped and depressed semicircles likely due to low ionic conductivity and high viscosity in concentrated solution, we did not fit the obtained Nyquist plots to obtain R_{HF} and R_{LF} values and rather chose to discuss through the Nyquist plots to keep a rigorous discussion. After the 1st cycle charge-discharge (4.6 – 2.0 V_{Li}, charge sequence coupled with EIS) at C/10 was performed in a three-electrode configuration, faster cycling tests (2nd-99th cycle) were then conducted with a two-electrode configuration (NMC811 as working electrode and Li metal as counter electrode) with CCCV - constant current (1C) / constant voltage (cut-off current at 0.05C) – charging condition and 1C discharge condition with cut-off potential between 4.6 V_{Li} and 2.0 V_{Li}. At the 100th cycle, three-electrode 0.1C charge-discharge with EIS measurement was conducted again to evaluate resistance growth compared with the 1st cycle. After the 101st cycle, two-electrode fast cycling with CCCV condition (1C-0.05C for charge, 1C for discharge) was conducted again. The 1st and 100th three-electrode cycling with EIS measurement was conducted at 25 ^oC in an environmental

chamber (SU-241, Espec) and fast two-electrode cycling (2-99th cycle and after 101th cycle) was conducted at room temperature. Coin-cell cycling was also conducted as previously reported.[37]

Raman spectroscopy Raman spectra of the electrolyte solutions and charged pellet electrodes were measured using a microscope Raman spectrometer system (LabRAM HR, Horiba) with 532 and 632 nm laser excitations, which was calibrated using a silicon standard. All the pellet electrodes and most of the electrolyte solution samples were measured with 532 nm laser excitation unless otherwise noted. The spectra were accumulated 5 times (pellet electrode) or 10 times (electrolyte solution sample) to achieve a sufficiently high signal-to-noise ratio. Detail Raman sample preparation method can be found in the previous report.[14] For solution samples, after baseline correction of the entire spectral range, the integrated intensity (area) in the wave number range of 850 – 920 cm^{-1} (including both free- and bound-EC, and EMC band) was normalized. The Raman spectra of the solutions were deconvoluted using a Gaussian-Lorentzian (pseudo-Voigt) function as shown in **Figure S2**. The molar fraction of free/bound species was computed from integral intensities of corresponding Raman peaks. Assuming that Raman scattering coefficients for free- and bound-carbonate are identical and constant in the whole concentration range[93], $I_{\text{bound-EC}} / I_{\text{total-EC}}$, $I_{\text{bound-EMC}} / I_{\text{total-EMC}}$ and the concentration of $LiPF_6$ in the solution were related to the molar fraction of free/bound species using the following:

$$\frac{I_{bound-EC}}{I_{free-EC} + I_{bound-EC}} = \frac{c_{bound-EC}}{c_{EC}} = \frac{n_{EC} \cdot c_{LiPF6}}{c_{EC}}$$

$$\frac{I_{bound-EMC}}{I_{free-EMC} + I_{bound-EMC}} = \frac{c_{bound-EMC}}{c_{EMC}} = \frac{n_{EMC} \cdot c_{LiPF6}}{c_{EMC}}$$

$$n_{EC} + n_{EMC} = n_{total}$$

Where c_{EC} and c_{EMC} [M] are the molar concentration of EC and EMC, $c_{bound\text{-}EC}$ and $c_{bound\text{-}EMC}$ [M] are the concentration of bound-EC and bound-EMC, c_{LiPF6} [M] is the concentration of $LiPF_6$, n_{EC} and n_{EMC} are the number of solvated EC and EMC per one Li^+ ($c_{bound\text{-}EC}/c_{Li+}$ or Li^+:bound-EC = 1:n_{EC}) and $c_{bound\text{-}EMC}/c_{LiPF6}$ (Li^+:bound-EMC = 1:n_{EMC}), respectively, and n_{total} is the total solvation number of Li^+ from both EC and EMC. Herein, I_{bound} / I_{total} is the same as c_{bound} / c_{total}. It should be noted that EC:EMC of 30:70 wt/wt corresponds to 33.6:66.4 mol/mol.

FT-IR spectroscopy The Fourier transform infrared (FT-IR) spectra of the materials were obtained on an FT-IR Tensor II (Bruker) equipped with a deuterated triglycine sulfate (DTGS) detector inside an argon-filled glovebox. The species formed on the active material during (electro)chemical processes were analyzed with the diffuse reflectance infrared Fourier transform (DRIFT) accessory (Praying Mantis, Harrick scientific products). Detailed experimental condition can be found elsewhere.[14] All FTIR spectra of the liquid samples were recorded using a single reflection attenuated total reflection (ATR) accessory (Pike Vee-Max II, Pike Technologies) with a Ge prism (Pier optics) at an incident angle of 45 degrees.

X-ray photoelectron spectroscopy (XPS) measurements All the XPS spectra were collected using a PHI 5000 VersaProbe II (ULVAC-PHI, INC.) using a monochromatized Al K_α source and a charge neutralizer. Detail procedures can be found in the previous publication.[14] Adventitious carbon at 285 eV (C1s spectra) was used for calibration of all XPS spectra. The chemical compositions, binding energies and full width at half maximum of all spectra can be found in **Tables S4 –S7**.

2.2 Computational methods

Raman – FTIR simulations The Raman and FTIR spectra where simulated by computing the vibrational frequencies of solvent molecules, salt ions and solvent-ions complexes in an implicit solvation model (PCM[9]), and dimethyl sulfoxide (DMSO, dielectric constant $\varepsilon = 47$) was used as solvent. We used the B3LYP functional and 6-311++G** basis set, as implemented in the Gaussian (g09) suite[94].

Interaction/adsorption energy calculations The EC C-H bond dissociation energy and the interaction energy of Li^+ with EC were estimated by considering complexes of one Li ion with 1-4 EC molecules in vacuum and in implicit DMSO solvent. We used the B3LYP functional for EC bond dissociation energy and Perdew Burke-Enzerhof (PBE) functional for Li^+-EC interaction[95] and 6-31+G* basis set.

The adsorption energy of EC on the surface of $LiMO_2$ (M = Mn, Co and Ni) and Mn- and Co-doped $LiNiO_2$, and the thermodynamic reaction profiles for EC and Li $(EC)_3$ on $LiNiO_2$ were computed by periodic plane wave calculations, with projector augmented wave potentials, and PBE functional, as implemented in the Vienna ab initio simulation package (VASP).[96,97] We employed a DFT+U approach[98,99] with effective Hubbard U values U_{eff} = 4.0 eV for Mn, 3.3 eV for Co and 6.4 eV for Ni.[100,101] EC was adsorbed on the $(10\bar{1}4)$ surface, with a (4 × 2) surface unit cell and a five-layer slab, where the three bottom layers were kept fixed at the bulk positions, while the coordinates of the two uppermost layers and the adsorbates were fully relaxed. The slabs were separated by a vacuum layer of at least 13 Å. Additional details can be found in the previous work[16].

3. Results and Discussion

Salt-concentration-dependent Free-solvent activity

Concentration-dependent Raman spectra in the range from 850 to 965 cm^{-1} revealed the EC ring breathing modes with and without Li^+ coordination[14] and the O-CH_3/O-C_2H_5 stretching modes of EMC with and without Li^+ coordination,[67] as shown in **Figure 1 (a)**. Pure EC/EMC (30/70 wt%) solution show one sharp band at ~892 cm^{-1}, corresponding to the EC ring breathing mode,[14] and one broad band centered at ~935 cm^{-1}, corresponding to the O-CH_3/O-C_2H_5 stretching mode of EMC, where the nature of the broad band[93] most likely come from two peaks (~930 and ~938 cm^{-1}) due to the asymmetric structure of EMC. With increasing concentration of $LiPF_6$ in the solution, the band intensity of EC ring breathing (~892 cm^{-1}) was found to decrease monotonically, which was replaced gradually by another sharp band at a higher wavenumber (~904 cm^{-1}), with a clear isosbestic point at ~899 cm^{-1}. Similarly, the band intensity of O-CH_3/O-C_2H_5 stretching in EMC (~935 cm^{-1}) was reduced gradually with increasing $LiPF_6$ concentration, which was coupled with the appearance and growth of another broad band at ~946 cm^{-1} with a clear isosbestic point at ~940 cm^{-1}. These two new bands centered at ~904 and ~946 cm^{-1} can be assigned to Li^+-coordinated-EC and EMC. No visible change was found for the peak centered at ~ 880 cm^{-1} that is associated with EMC molecules (can be seen in pure solvent spectrum, **Figure S3**), which will not be discussed further. Moreover, the appearance and growth of Li^+-coordinated-EC and -EMC bands with increasing $LiPF_6$ concentration were accompanied with increasing intensity of a new band centered at ~742 cm^{-1}, which can be attributed to the P-F symmetric stretching vibration of PF_6^-[102], as shown in **Figure 1(b)**. At $LiPF_6$ concentrations greater than Li:Carbonate = 1:5 (2.0 M), a peak shoulder at the high wavenumber side appeared, indicating the formation of complexes between Li ions and PF_6^- anions or contact ion pair (CIP). With increasing $LiPF_6$ concentration,

the distance between the anions and cations decreases in the solutions and ion-pair formation/aggregation occurs.[53] Therefore, the band at ~742 cm^{-1} was deconvoluted into one component of free PF_6^- at ~742 cm^{-1} at concentrations below Li:Carbonate = 1:5 (2.0 M) while above, two different components, free PF_6- at ~742 cm^{-1} and Li^+-bound PF_6 at ~744 cm^{-1} were obtained (see details in **Figure S2**), which later increased with increasing $LiPF_6$ concentration.

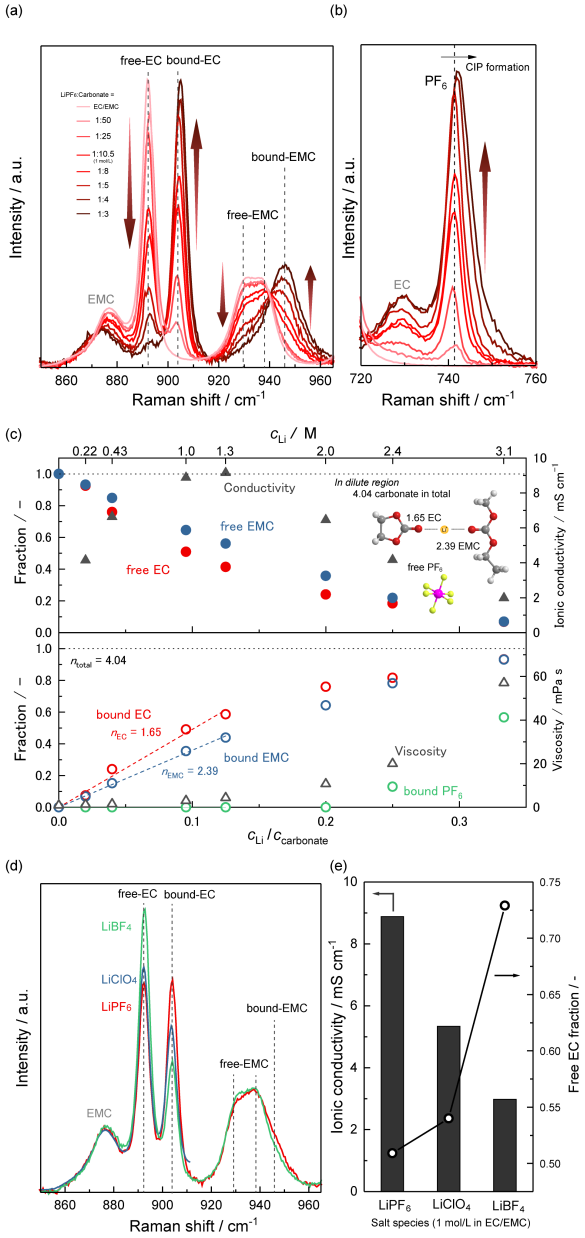

Figure 1 Normalized Raman spectra of $LiPF_6$ in EC:EMC (3:7 wt/wt) solution in the range (a) carbonate bands (850 -965 cm^{-1}) and (b) PF_6- band (700-760 cm^{-1}) measured at 25 °C. (c) Ionic conductivity, viscosity and estimated molar fractions of free/bound-EC, free/bound-EMC ($I_{free\text{-}EC}$/ $I_{total\text{-}EC}$, $I_{free\text{-}EMC}$/ $I_{total\text{-}EMC}$), and Li^+-bound PF_6^- ($I_{bound\text{-}PF6}$ / $I_{total\text{-}PF6}$) in the $LiPF_6$ in EC/EMC solution based on the ratio of integral intensities of Raman peaks. All the R^2 values for the deconvolution are higher than 0.987 and linear fits for calculating solvation number are higher than 0.992. Detail deconvoluted spectra were shown in **Figure S2**. (d) Normalized Raman spectra of 1.0 M $LiPF_6$, ClO_4 and BF_4 in EC:EMC (30:70 wt%) solution in the range 850 -965 cm^{-1} (carbonate bands) measured at 25 °C. Note that the region higher than 910 cm^{-1} for $LiClO_4$ sample was removed due to severe overlap of ClO_4 peak and EMC peak. (e) Ionic conductivity and free EC fraction in 1.0 M $LiPF_6$, ClO_4 and BF_4 in EC:EMC (3:7wt) solution.

The fractions of carbonates and PF_6 anions with and without Li^+ coordination were quantified from integrated intensities (I) of corresponding Raman bands, where Raman scattering coefficients for free- and bound Carbonates were assumed to be identical and constant.[77,93] **Figure 1(c)** shows that the fractions of free-EC and free-EMC decrease while the fraction of Li^+-coordinated EC and EMC increases monotonically with increasing molar ratio of $LiPF_6$/Carbonate ($c_{Li}/c_{Ccarbonate}$), which were obtained from the ratios of I_{free}/I_{total} and I_{bound}/I_{total}, respectively. The fraction of Li^+-bound EC is higher than that of Li^+-bound EMC, which is consistent with having much higher polarity of EC (dielectric constant of 90[103]) compared to EMC (dielectric constant of 3[103]). Of significance to note is that the molar fractions of free EC and EMC were very small (combined fractions equal to ~0.07 or ~7 mol%) for the most concentrated solution of $LiPF_6$/Carbonate of 1:3 (3.1 M), indicating negligible free solvent activity, in comparison to that of the conventional electrolyte concentration of 1.0 M (0.5 or 50 mol%). The fraction dependence of Li^+-bound EC and EC on the molar ratio of $LiPF_6$/Carbonate (the slope in **Figure 1c**) was used to estimate the solvation number of Li^+, which fitting was limited to concentrations below Li:Carbonate = 1:5 (2.0 M) where $LiPF_6$ is fully dissociative (Figure 1b). Li^+ was found to be coordinated by ~1.6 for EC and ~2.4 for EMC, giving rise to a total solvation number of ~4, which is in agreement with previous reports of Li^+ solvation numbers around 4.[75,81,104] The result is further

supported by having negligible fractions of Li^+-bound PF_6^- at concentrations below Li:Carbonate = 1:5 (2.0 M) estimated from the integrated intensities of free (~742 cm^{-1}) and bound PF_6^- (~744 cm^{-1}) components (**Figure 1b**), which is consistent with the highly dissociative nature of PF_6^- anions. At higher concentrations, 0.13 and 0.57 of PF_6^- interacted directly with Li^+ for Li:Carbonate ratios of 1:4 (2.4 M) and 1:3 (3.1 M), indicating stronger CIP formation/aggregation. Therefore, Raman spectroscopy reveals that Li^+ is coordinated as $[Li(EC)_{1.64}(EMC)_{2.37}]^+$ in the EC:EMC (3:7 wt/wt or 1:2 mol/mol) solutions with $LiPF_6$ concentrations equal to or less than 2.0 M. In contrast, at the highest concentration having Li:Carbonate of 1:3 (3.1 M), nearly all the EC and EMC (>93 mol%) are coordinating to Li^+ and more than half of PF_6^- is also participating Li^+ solvation, giving rise to complexes resembling $[Li(EC)_1(EMC)_2(PF_6)]$ and $[Li(EC)_1(EMC)_2]^+$.

Replacing more dissociative $LiPF_6$ with less dissociative $LiBF_4$, the Li-coordinated EC ring breathing mode feature (~904 cm^{-1}) was found to decrease in intensity while that of the free EC ring breathing band (~892 cm^{-1}) increased, indicating an increased fraction of free EC molecules. As solvent and anion (both Lewis bases) are competing with each other to solvate (interact) to Li^+ (strong Lewis acid) in the electrolyte solution,[81,105] fully dissociative PF_6^- at 1.0 M (**Figure 1b**) does not disturb the solvation of Li^+ by carbonate molecules whereas less dissociative BF_4^- can bind with lithium ions and results in more free carbonate solvents. The B-F stretching mode of 1.0 M $LiBF_4$ in EC/EMC solution (**Figure S4**) shows free-BF_4^- at 776 cm^{-1} and Li^+-bound -BF_4^- at 774 cm^{-1},[47] which intensity was used to quantify Li^+-bound-BF_4^- as 0.26 or 26 mol% in the 1.0 M EC/EMC (30/70 w/w%) electrolyte. Further support of more free solvent molecules in 1.0 M BF_4^- electrolyte came from ATR measurements (**Figure S5**), which shows the Li-coordinated EC and EMC C=O features (1774 cm^{-1} and 1720 cm^{-1}) both increase in intensity relative to free EC (1807 cm^{-1}) and EMC C=O (1744 cm^{-1}) features. By integrating the free EC

(892 cm^{-1}) and Li-coordinated EC (904 cm^{-1}) band intensities in the Raman spectra of 1.0 M $LiBF_4$ electrolyte, we further quantified the fraction of free EC compared to Li^+-coordinated EC in **Figure 1e**, which revealed a higher fraction of free EC by replacing $LiPF_6$ (0.51) with $LiBF_4$ (0.73).

The ionic conductivity was found to first increase with greater $LiPF_6$ concentration and then decrease at concentrations greater than (up to 1.3 M), as shown in **Figure 1c**. This nonlinear concentration-dependent conductivity trend is similar to those found previously for non-aqueous electrolyte solutions with ether[55,60,61,106,107], carbonate[67] and other solvents.[70,75] The maximum conductivity found for concentrations at ~1 M can be explained by increasing charge carrier concentrations including $[Li(EC)_{1.64}(EMC)_{2.37}]^+$ and PF_6^- but reduced ion mobility at concentrations greater than 1.3 M (**Figure 1c**). The proposed ion mobility reduction is supported by markedly increased electrolyte viscosity (**Figure 1c**), which results from electrostatic drag associated with solvated lithium ions, $[Li(EC)_1(EMC)_2]^+$ and PF_6^- and the formation of ion-paired complexes, $[Li(EC)_1(EMC)_2(PF_6)]$. These two competing effects result in a maximum ionic conductivity at around 1 M.[61,75,107,108] Moreover, the change in the solvation structure directly affects the change in the ionic conductivity due to a decrease in change carrier (Li^+) concentration through the formation of ion-pair (neutral) species, where $LiPF_6$ has the highest conductivity and lowest free-carbonate activity (*i.e.* highest dissociation) compared to $LiClO_4$ and $LiBF_4$ salt with the same concentration, due to stronger aggregation of those more Lewis basic anions (BF_4^- and ClO_4^-) to Li^+.

The influence of Free-solvent activity on the cycling stability of Ni-rich NMC811

Using the most concentrated electrolyte (3.1 M $LiPF_6$ in EC/EMC) with negligible free solvent molecules (**Figure 1c**) led to enhanced capacity retention of NMC811 upon cycling

compared to electrolytes with lower $LiPF_6$ concentrations (1.0 and 2.0 M $LiPF_6$ in EC/EMC), as shown in Figure 2a. NMC811 was found to have comparable initial discharge capacities of ~220 mAh g^{-1} (C/10 and charged to 4.6 V_{Li}) and ~200 mAh g^{-1} (1 C and 4.6 V_{Li}) among all the electrolytes tested in this study. Much greater capacity retention was found for the most concentrated electrolyte upon subsequent cycling at 1 C than the other electrolytes with lower $LiPF_6$ concentrations (1.0 and 2.0 M $LiPF_6$ in EC/EMC in **Figure 2a**). The greater discharge capacities of NMC811 cycled in the most concentrated electrolyte (215 mAh g^{-1} in **Figure 2a**) were confirmed at C/10 after 100 cycles than those tested in 2.0 M (175 $mAhg^{-1}$) and 1.0 M (163 $mAhg^{-1}$). After 500 cycles (1 C and 4.6 V_{Li}), the most concentrated electrolyte (3.1 M) shows reversible capacity ~150 mAh g^{-1} or ~75% capacity retention while the other electrolytes with lower $LiPF_6$ concentrations (1.0 and 2.0 M $LiPF_6$ in EC/EMC) had electrode capacity fading below 100 mAh g^{-1}. Similar capacity loss was found for cycling NMC811 in EC-only or EMC-only electrolytes such as 1.5 M $LiPF_6$ in EC (1.5 M $LiPF_6$ in EC is liquid and 1.0 M $LiPF_6$ in EC is solid) and EMC-only (1.0 M $LiPF_6$ in EMC） in **Figure S7** to that of 1.0 M $LiPF_6$ in EC/EMC. The greater capacity retention with the most concentrated electrolyte was further shown for cycling NMC811 at 1 C to 4.4 V_{Li} than the electrolyte with 1.0 M $LiPF_6$ (**Figure S8**). Moreover, the Coulombic efficiency of NMC811 (quantified as the ratio of discharge capacity over charge capacity, 99.7% averaged from the 3rd to 100th cycle) in the most concentrated electrolyte (3.1 M) was greater than the other electrolytes with lower concentrations (98.9% in 1.0 M and 98.6% in 2.0 M), as shown in **Figure S9**. These observations suggest that reducing free carbonate activity by replacing free EC or EMC by Li^+-coordinated EC or EMC can lead to enhanced capacity retention and Columbic efficiency upon cycling of NMC811 in the 3.1 M (0.07 fraction of both free EC and EMC) than that of the 1.0 M $LiPF_6$ (0.51 and 0.65 fraction of free EC and EMC,

respectively) electrolyte. The greater capacity retention of NMC811 cycled in the 3.1 M $LiPF_6$ electrolyte is accompanied with smaller impedance growth as reflected by lower gaps between charge and discharge voltages during cycling (**Figure 2b)** in comparison to that cycled in the 1.0 M $LiPF_6$ electrolyte (**Figure 2c**). The charge and discharge voltage profiles and discharge capacity at the 50th cycle (red in **Figure 2b**) were comparable to those of the 3rd cycle in the 3.1 M electrolyte. In contrast, the charge and discharge voltage profiles were altered considerably with the 1.0 M electrolyte in comparison to those of the 3rd cycle, showing nearly four times greater voltage polarization, and much lower discharge capacity than that of the 3rd cycle.

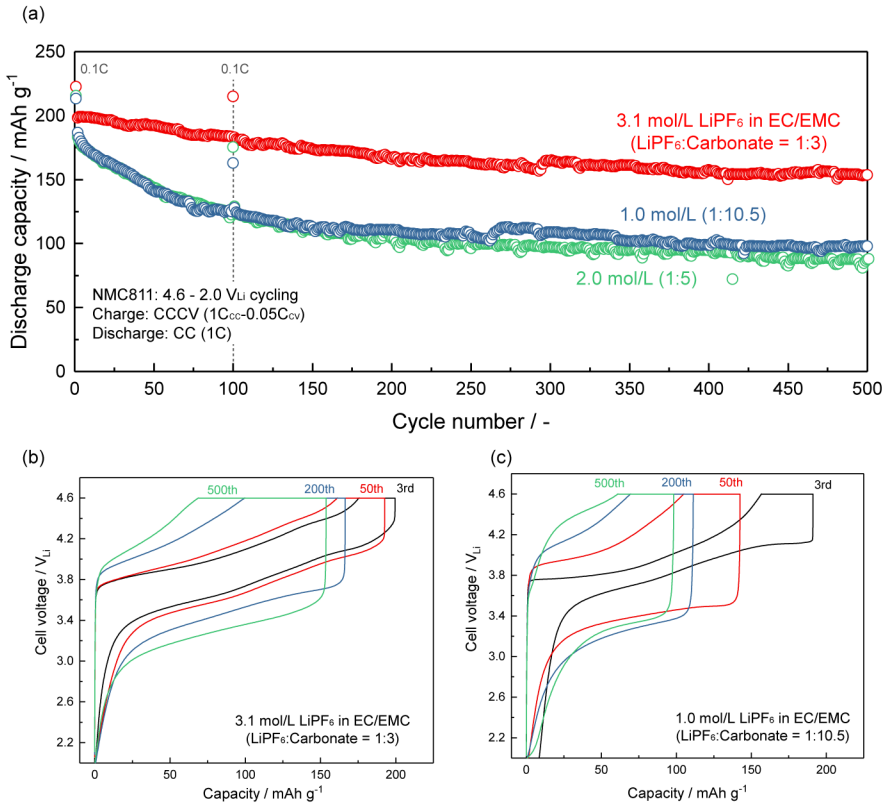

Figure 2 Cycling performance of NMC811 composite electrodes with different electrolyte solutions. (a) The discharge capacity and charge-discharge profile with (b) 3.1 M $LiPF_6$ in EC/EMC and (c) 1.0 M $LiPF_6$ in EC/EMC upon charging to 4.6 V_{Li}. At the 1st and 100th cycle, the cells were measured in a three-electrode configuration, which composed of NMC811|$Li_4Ti_5O_{12}$-mesh|Li (see experimental section in detail), galvanostatically charged at 27.5 mA/g (C/10) and subject to EIS measurements (Nyquist plots are available in **Figure 3**). From the 2nd to the 99th cycle and after 101st cycle, the cells were tested with a two-electrode configuration that consisted NMC811 as the working electrode and Li metal as the counter electrode upon cycling between 4.6

and 2.0 V_{Li}, which included first charging to 4.6 V_{Li} under 1C, subsequently voltage holding at 4.6 V_{Li} until the current reached C/20, then discharging at 1C to 2.0 V_{Li}.

EIS measurements of NMC811 composite electrodes in the NMC811|$Li_4Ti_5O_{12}$-mesh|Li three-electrode cells obtained in the 1st and 100th cycles at C/10 further supported smaller impedance growth during cycling in the most concentrated electrolyte (3.1 M) than that of 1.0 M. As shown in **Figure 3**, two semicircles were observed in the Nyquist plots for Li intercalation into composite electrodes like previous work.[58,109] The high-frequency semicircle (left, 10^3 – 10^4 Hz) has been assigned to impedance at the electrified interface (predominantly lithium ion migration and adsorption/desorption in the pore structure of composite electrode[58]) while the low-frequency semicircle (right, 10^0 – 10^1 Hz)) corresponds to the combination of charge transfer resistance at the electrode-electrolyte interface (equivalent circuit can be found in the inset of **Figure 3c**).[58] In the first cycle, although a higher resistance was observed for the low-frequency semicircle (10^0 – 10^1 Hz) in the most concentrated solution compared to 1.0 M solution (**Figure 3ab**) at 4.0 V_{Li}, suggesting greater charge-transfer resistance[58] in 3.1 M solution, a smaller increase in the low-frequency impedance was found with increasing potential from 4.0 to 4.5 V_{Li} for the 3.1 M than the 1.0 M electrolyte. It is interesting to note in **Figure 3a**, high-frequency resistance (10^3 – 10^4 Hz) and low-frequency resistance (10^0 – 10^1 Hz) were comparable below 4.2 V_{Li} while R_{LF} suddenly became ~10 times larger when the potential increased from 4.2 to 4.3 V_{Li}, indicating severe resistance growth on the NMC811 surface in the 1.0 M electrolyte, which is consistent with greater capacity loss upon cycling to 4.3 V_{Li} and greater. [110] At the 100th cycle (**Figure 3cd**), the low-frequency impedance with 3.1 M solution grew slightly (~100 Ω at 4.0 V_{Li}) and exhibited comparable potential dependence to that in the first cycle. In contrast, the low-frequency (charge transfer) impedance with 1.0 M grew significantly after 100 cycles, where the potential

dependence of the impedance observed in the first cycle disappeared. These observations are in agreement with higher capacity retention and lower overpotential observed during cycling in the most concentrated electrolyte (3.1 M) compared to electrolytes of lower salt concentrations shown in **Figure 2**. Although the cycling experiments were carried out with two-electrode configuration, this three-electrode EIS results clearly shows that the capacity decay is mainly caused by NMC positive electrode side. In addition, two-electrode cell cycling of Li/NMC111 in the conventional electrolyte: 1 M $LiPF_6$ in EC:EMC has much reduced capacity loss than that of Li/NMC811 in this work and in previous work,[9,111] indicating that the lithium metal electrode and its interfacial changes during cycling is not responsible for large capacity loss noted for Li/NMC811. Further support came from EIS measurements of potential holds at 4.4 V_{Li} for 100 hours in the 3.1 M and 1.0 M $LiPF_6$ electrolytes, shown in **Figure S10**. Both high-frequency and low-frequency impedances were found not to change with time for 100 hours with the 3.1 M $LiPF_6$ EC/EMC electrolyte shown in **Figure S10b**, which is consistent with the higher capacity retention in cycling results (**Figure 2a**). On the other hand, the low-frequency impedance was found to continuously increase with time in the 1.0 M electrolyte while there was no significant changes for the high-frequency impedance upon a potential hold at 4.4 V_{Li} (**Figure S10a**), which is in agreement with the assignment of high-frequency impedance to the electrified interface resistance associated with ion adsorption and desorption in the composite pore structure. Not only did NMC811 show a much greater low-frequency impedance of ~400 Ω under comparable conditions to that of other positive electrode materials such as composite Li_xCoO_2 (~20 Ω) for R_{LF} at 4.4 V_{Li},[58] but the low-frequency impedance also increased sharply with time in **Figure S10a**, which is consistent with capacity loss and overpotential growth during cycling shown in **Figure 2b** and **Figure 2c**, respectively. The bulk resistances in concentrated electrolyte (3.1 M solution) and 1.0 M solution are ~10 ohm and

~3 ohm, respectively, while the charge-transfer resistances in both electrolytes are ~200 ohm at 4.3 V_{Li} at the first cycle and increase over cycling (**Figure 3**). Thus, the rate limiting step of this system would be the charge transfer reaction at the NMC811-electrolyte interface.

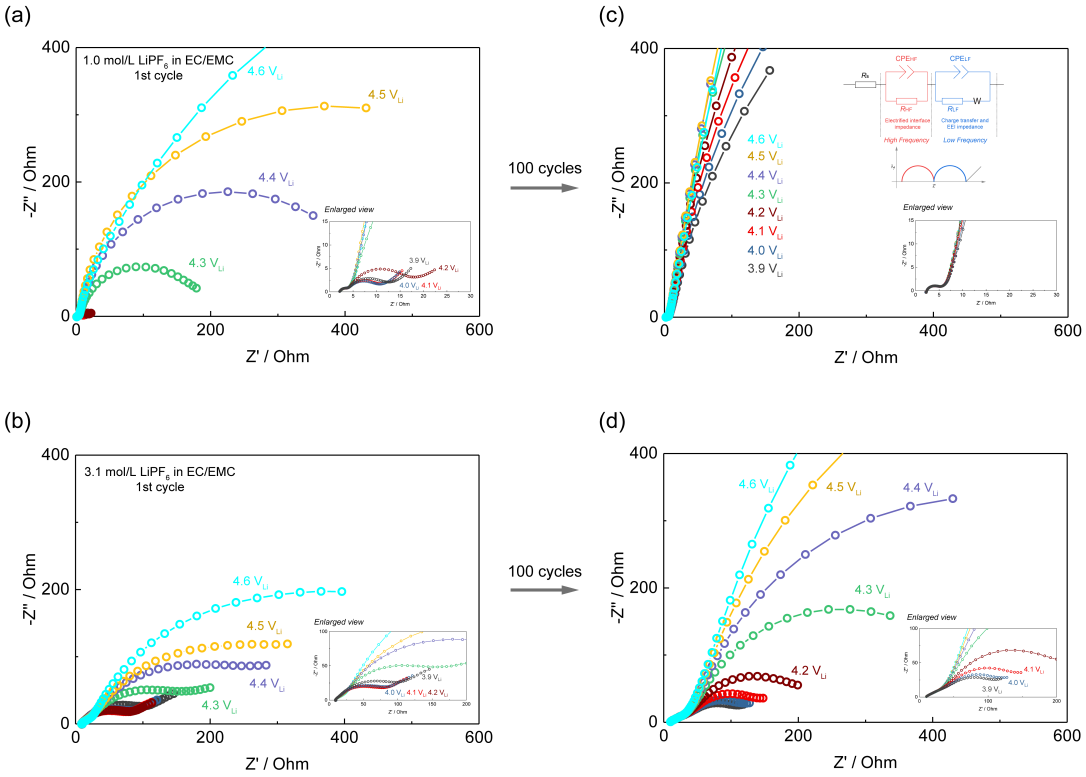

Figure 3 Nyquist plots for EIS measurement on NMC811 composite electrode in NMC811|$Li_4Ti_5O_{12}$-mesh|Li three electrode cell with 1.0 M $LiPF_6$ / EC-EMC (3:7 wt/wt) at (a) 1st cycle and (b) 100th cycle, and with 3.1 M $LiPF_6$ / EC-EMC (3:7 wt/wt) at (c) 1st cycle and (d) 100th cycle at different potential at 25 °C. At 1st and 100th cycle, the cell was operated with three-electrode configuration and galvanostatically charged at 27.5 mA/g (0.1C) and hold potential for 1 hour at each potential (3.9, 4.0, 4.1, 4.2, 4.3, 4.4, 4.5 and 4.6 V_{Li}), then relax 1 hour before EIS sequence. From 2nd to 99th cycle, the cell was operated with two-electrode configuration (NMC811 as working electrode and Li metal as counter electrode) and cycle between 4.6 and 2.0 V_{Li} with CCCV condition (1C charge to 4.6 V_{Li} and hold at 4.6 V_{Li} until the current reach to C/20, then discharge at 1C to 2.0 V_{Li}, cycle performance can be found in **Figure 2**).

The influence of Free-solvent activity on the surface chemistry of cycled NMC811

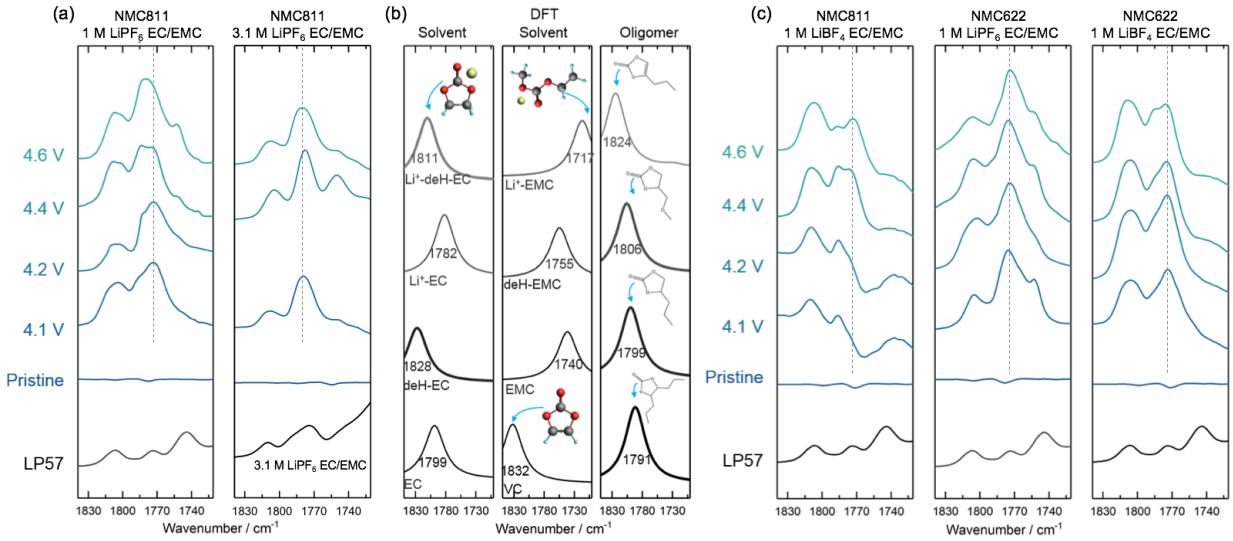

Figure 4 DRIFT spectra of (a) C=O stretching region for $Li_xNi_{0.8}Mn_{0.1}Co_{0.1}O_2$ (NMC811) for pristine pellets (no electrolyte exposure) and after charged to 4.1, 4.2, 4.4, and 4.6 V_{Li} in 1.0 M (=LP57) and 3.1 M $LiPF_6$ in EC/EMC (3:7 w:w). (b) Simulated FT-IR spectra of C=O vibration shown in EC, Li^+-coordinated EC, dehydrogenated EC (deH-EC), Li^+-coordinated dehydrogenated EC, EMC, vinylene carbonate (VC), and oligomers possibly formed through EC dehydrogenation (including, from top to bottom, $C_6H_8O_3$, $C_5H_8O_4$, $C_9H_{16}O_3$, $C_6H_{10}O_3$). (c) C=O stretching region for $Li_xNi_{0.6}Mn_{0.2}Co_{0.2}O_2$ (NMC622), and $Li_xNi_{0.8}Mn_{0.1}Co_{0.1}O_2$ (NMC811) for pristine pellets (no electrolyte exposure) and after charged to 4.1, 4.2, 4.4, and 4.6 V_{Li} in 1.0 M $LiPF_6$ in EC/EMC (3:7 w:w) and 1.0 M $LiBF_4$ in EC/EMC (3:7 w:w).The example electrochemistry profiles of NMC622, and 811 pellet electrodes in different electrolytes are shown in **Figure S11**.

To examine the reactivity of the electrolyte towards the NMC oxide surface, surface analysis for charged NMC was conducted via FT-IR DRIFT and XPS measurements. DRIFT measurements showed that there was a decrease in the oxide-electrolyte reactivity induced by a decrease of free

solvent by increasing $LiPF_6$ concentration. **Figure 4a** shows the C=O stretching region of pristine NMC 811 and charged electrodes to 4.1 V_{Li}, 4.2 V_{Li}, 4.4 V_{Li}, 4.6 V_{Li} from DRIFT measurements, and that of the pristine electrolyte (1.0 M $LiPF_6$ in EC/EMC 30/70 w/w%) from the ATR measurements, which comprises of three major peaks at ~1807, ~1773, and ~1744 cm^{-1}, corresponding to the C=O stretching mode of EC, Li^+-coordinated EC, and EMC, respectively.[14] Upon charging to 4.6 V_{Li} in 3.1 M, no visible blueshift was observed for the C=O stretching modes of NMC811, revealing no evidence of EC dehydrogenation on NMC 811 in the most concentrated region with low free-carbonate activity. In addition, Raman spectroscopy experiments for charged NMC811 pellet electrodes charged to 4.6 V_{Li} in 3.1 M $LiPF_6$ solution failed to detect characteristic peaks at ~732 cm^{-1} and 907 cm^{-1} attributed to dehydrogenated EC (ring distortion and ring breathing mode of dehydrogenated Li^+-EC, respectively)[14] (**Figure S13**), further supporting that the most concentrated electrolyte suppresses carbonate oxidative dissociation. In contrast, upon charging NMC811 to 4.2 V_{Li} in 1.0 M $LiPF_6$ in EC/EMC, a blueshift was observed for the peaks at 1807 and 1773 cm^{-1} which can be attributed to EC-derived species formed on charged oxide surfaces through the dehydrogenation of CH_2-hydrogen in EC.[14] This assignment is supported by the calculated spectra for the C=O stretching mode of dehydrogenated EC coordinated with Li^+ (1811 cm^{-1}) and/or oligomers derived from dehydrogenated EC such as $C_5H_8O_4$ (1806 cm^{-1}) and $C_6H_{10}O_3$ (1791 cm^{-1}) in **Figure 4b** (chemical structures of $C_5H_8O_4$ and $C_6H_{10}O_3$ are also shown). This blueshift cannot be attributed to EMC or EMC-derived features as C=O stretching of EMC (**Figure 4b** middle panel) is located at much lower wavenumbers (around 1740 cm^{-1}). In addition, as DRIFT is an ex-situ analysis after grinding charged pellet electrode with KBr, the bound carbonate and free carbonate can be exchanged during sample preparation. This would explain why bound EC exhibits a blue shift even if free carbonate is dehydrogenated. As further evidence,

a simple mixture of $LiPF_6$ and carbonates prepared with the same procedure showed a decrease in the free EC band and an increase in the Li^+-EC band, which indicates that there is an exchange between free/bound species during the grinding process. In summary, DRIFT spectra on charged electrodes revealed that with decreasing $LiPF_6$ concentration (increasing free-carbonate activity), we lowered the onset potential for solvent dissociative adsorption on oxide surfaces, and increased the solvent and oxide reactivity.

Switching from $LiPF_6$ to less dissociative $LiBF_4$ to have more free solvent molecules than Li^+-coordinated molecules, DRIFT measurements showed increased oxide-electrolyte reactivity with charged NMC622 and 811. Upon charging to 4.4 V_{Li} for NMC622 in 1.0 M $LiBF_4$ electrolyte, a blueshift is observed for the peaks at 1807 and 1773 cm^{-1} whereas no significant changes are observed for NMC622 even when charged to 4.6 V_{Li} in 1.0 M $LiPF_6$ electrolyte (**Figure 4c**). A similar blueshift is observed for NMC811 charged to 4.2 V_{Li} and above in $LiPF_6$ and charged to 4.1 V_{Li} and above in $LiBF_4$. Such blueshifts can be attributed to EC-derived species formed on charged oxide surfaces through the dehydrogenation of CH_2-hydrogen in EC.[14] This observation indicates that 1.0 M $LiBF_4$ electrolyte shows lower onset voltages for solvent dehydrogenation compared with more dissociative $LiPF_6$ on NMC622, as well as NMC811, supporting the argument that electrolytes with lower free-carbonate activity show increased stability against dehydrogenation on the oxide surface. This argument is in agreement with NMC811 cycled with 1.0 M $LiPF_6$ having greater capacity retention than 1.0 M $LiBF_4$ (**Figure S14**).

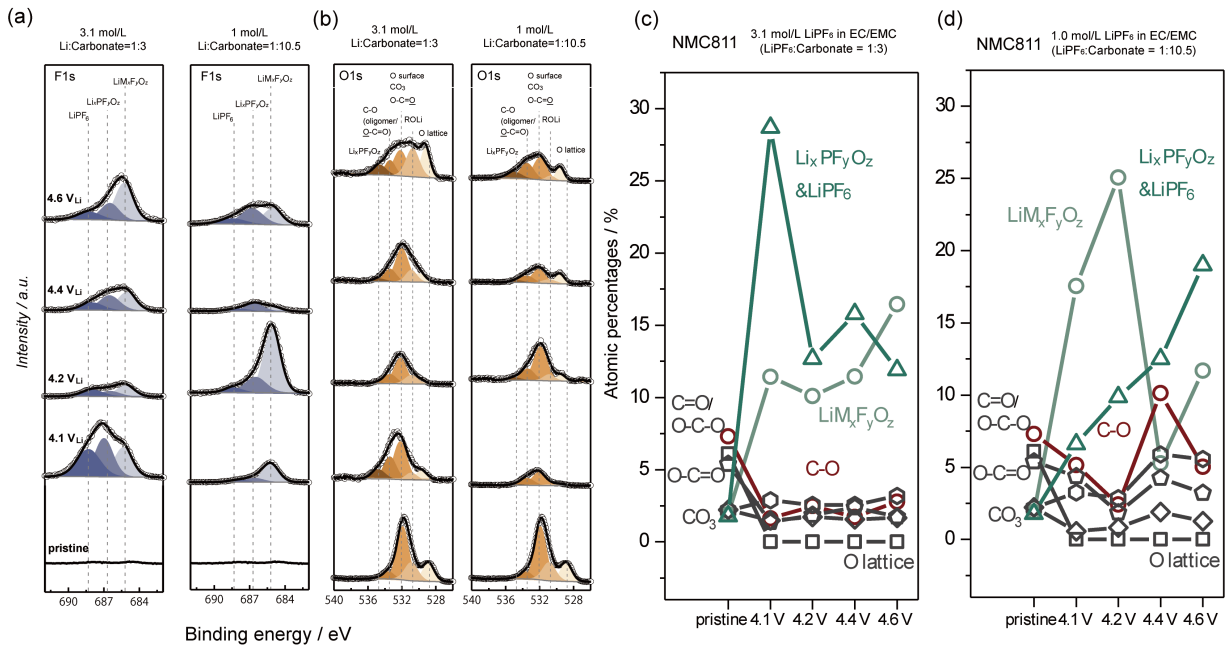

Figure 5 Concentration dependent XPS spectra of the (a) F1s and (b) O1s photoemission lines collected from carbon-free, binder-free NMC811 electrodes. C1s and P2p spectra are available in **Figure S15**. Atomic percentages from XPS spectra for the pristine and charged carbon-free, binder-free NMC811 electrodes in (c) 3.1 M $LiPF_6$ and (d) 1.0 M $LiPF_6$ in EC: EMC 3:7 (wt:wt). The electrodes were charged to 4.1, 4.2, 4.4 and 4.6 V_{Li} at 2.75 mA/g (C/100) and held at the given potential for 5 hours using 1.0 M $LiPF_6$ in EC: EMC (3:7 wt:wt) and 3.1 M $LiPF_6$ in EC: EMC (3:7 wt:wt) solution and compared with pristine electrodes. All the spectra were normalized by fixing the C1s photoemission peak of adventitious carbon (285 eV). The example electrochemistry profiles of NMC811 carbon-free binder-free powder electrodes are shown in **Figure S16**.

The increased electrolyte stability with decreasing free solvent activity is further supported by XPS results. XPS spectra of F 1s and O 1s (**Figure 5ab**) along with C1s, P2p, Ni2p, Co2p, Mn2p, Li1s/Co3p spectra (**Figure S15** and **Figure S17)** were collected from carbon-free, binder-free NMC811 electrodes charged to different potentials of the first charge in the 3.1 and 1.0 M $LiPF_6$ electrolyte. The F1s spectra can be deconvoluted into three species: metal fluorides/oxyfluorides ($LiM_xF_yO_z$) around 685.1 eV, $Li_xPF_yO_z$ species around 686.6 eV and $LiPF_6$ salt at 688.3 eV.[14] O1s spectra were also fitted to components at 529.3 eV, 531 eV, 532 eV, 533.4 eV, which can be attributed to O lattice[17,112,113], ROLi (semicarbonate and polyether species) [114,115],

semicarbonates ($ROCO_2Li$) with the CO_3 group[116,117], O-C=O bond as in esters or single bond between a carbon and oxygen (C-O) like in polyethers[112,114,118]. NMC811 electrodes charged to 4.1 and 4.2 V_{Li} in the 3.1 M $LiPF_6$ electrolyte were found to have less coverage of $LiM_xF_yO_z$ (685.1 eV)[14] and more coverage of $Li_xPF_yO_z$ (686.6 eV) and/or $LiPF_6$ (688.3 eV) in the F1s spectra (**Figure 5a**) relative to those charged in the 1.0 M $LiPF_6$ electrolyte (**Figure 5a**). This observation is in agreement with the lower oxygen lattice component of $LiM_xF_yO_z$ (529.3 eV,[14] **Figure 5b**) than oxygenated species such as $Li_xPF_yO_z$ (534.8 eV, **Figure 5b**) in the O1s spectra relative to those found for the 1.0 M $LiPF_6$ electrolyte,[14,17,37] where the O lattice peak of $LiM_xF_yO_z$ (529.3 eV,[14] **Figure 5b**) for charged NMC811 in both electrolytes was shifted to higher binding energy together with greater binding energy of the Ni2p peak (**Figure S17**) with increasing charging voltage. As the formation of lithium nickel oxyfluoride ($LiM_xF_yO_z$) has been attributed to oxide-mediated electrolyte oxidation,[14,17] specifically reactions among charged NMC811, $LiPF_6$ and protic species resulted from EC dehydrogenation on charged NMC811[14,17], these XPS results suggest that charged NMC811 in the 3.1 M electrolyte is more stable against oxide-mediated electrolyte oxidation[14,17] up to 4.2 V. This hypothesis is supported by much less coverage of oxidized carbon species such as C-O (**Figure 5b-d**) found on charged NMC811 in the 3.1 M electrolyte than the 1.0 M electrolyte, indicative of the oxidation of carbonate solvents. Unfortunately, with an increase in voltage to 4.6 V_{Li}, the intensity of $LiM_xF_yO_z$ (685.1 eV) in the F1s (**Figure 5a** and **Figure 5cd**) edge became greater for charged NMC811 in the 3.1 M $LiPF_6$ electrolyte, indicating greater reactivity with the electrolyte than for voltages 4.2 V and lower. Nevertheless, XPS results of charged NMC811 in the 3.1 M electrolyte (7% free solvents) to 4.2 V and lower, showing less coverage of lithium metal oxyfluorides and oxidized carbon species than that in the 1.0 M electrolyte (~50% free solvents), support that lithium-coordinated carbonate

solvents are more stable against oxide-mediated dehydrogenation and electrolyte oxidation than free carbonate solvents.

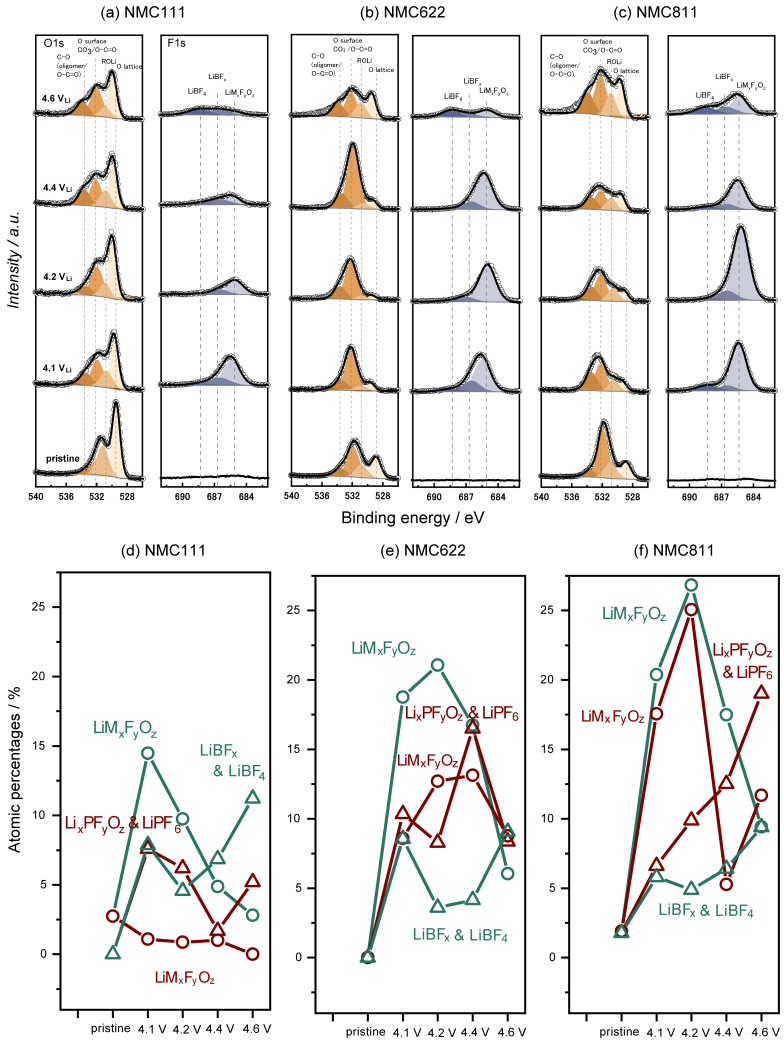

Figure 6 XPS spectra of the O1s and F1s photoemission lines for NMC111 (a), NMC622 (b) an NMC811 (c) for the pristine carbon-free, binder-free electrodes and after charging to 4.1, 4.2, 4.4, and 4.6 V_{Li} with 1.0 M $LiBF_4$ in EC: EMC (3:7 wt:wt) electrolyte. The C1s, B1s, Co2p, Mn2p, Ni2p and Li1s/Co3p XPS spectra is shown in **Figure S18**, **Figure S19** and **Figure S20**. Atomic percentages from XPS spectra for F in metal fluorides/oxyfluorides, $LiBF_x$ and $LiPF_yO_z$ (from F1s region) in the pristine and charged carbon-free, binder-free (d) NMC111, (e) NMC622 and (f) NMC811 electrodes at 4.1, 4.2, 4.4 and 4.6 V_{Li} using 1.0 M $LiPF_6$ or $LiBF_4$ in EC: EMC 3:7 (wt:wt). Other atomic percentages are available in **Figure S21**. The deconvolution parameters are shown in **Table S5**, **Table S6** and **Table S7**. The representative electrochemical profile is shown in **Figure S22**. The original spectra in 1.0 M $LiPF_6$ electrolyte are available in previous publication.[14]

Further support for the stability of lithium-coordinated carbonate solvent molecules against oxide-mediated dehydrogenation and electrolyte oxidation compared to free carbonate molecules came from XPS results of charged NMC111, 622 and 811 in a 1.0 M $LiBF_4$ electrolyte, which has more free solvent molecules than 1.0 M $LiPF_6$ (**Figure 1e**). XPS analysis of O1s and F1s spectra (**Figure 6a-c** along with C1s, B1s, Mn2p, Ni2p, Co2p and Li1s/Co3p) of carbon-free, binder-free NMC 111, 622 and 811 electrodes charged to 4.1, 4.2, 4.4 and 4.6 V_{Li} in 1.0 M $LiBF_4$ EC/EMC electrolyte (**Figure S18**, **Figure S19** and **Figure S20**) were compared to those charged in 1.0 M $LiPF_6$ EC/EMC electrolytes as reported previously.[14] The F1s spectra can be deconvoluted to three species: metal fluorides/oxyfluorides ($LiM_xF_yO_z$) around 685 eV[14,112], $LiBF_x$ species around 686.5 eV[87] and $LiBF_4$ salt at 688.5 eV.[87] The F1s intensity of NMC 111 charged with $LiBF_4$ electrolyte is higher than NMC 111 charged with $LiPF_6$ electrolyte (**Figure 6**) suggesting greater reactivity with BF_4^- than PF_6^- associated with EC dehydrogenation with the 1.0 M $LiBF_4$ electrolyte (with more free solvents, 73%). This argument is supported by the Ni2p and O1s spectra of NMC 111 charged with $LiBF_4$ electrolyte, where the Ni2p spectra shifted to higher binding energy from 854.5 eV to 856.0 eV with increasing potential, indicating the formation of lithium nickel oxyfluoride species,[14] and the O lattice peak shift to higher binding energy with increasing potential. Similarly, NMC 622 charged in 1.0 M $LiBF_4$ electrolyte revealed higher intensity of $LiM_xF_yO_z$-like species than NMC 622 charged with the $LiPF_6$ electrolyte whereas the $LiM_xF_yO_z$-like species have comparable atomic percentages for NMC 811 charged with $LiBF_4$ and $LiPF_6$ electrolyte. This observation is consistent with the differences noted in the C=O region of the DRIFT spectra of NMC622 and 811 charged with $LiBF_4$ and $LiPF_6$ electrolytes. While DRIFT spectra of NMC622 charged with $LiBF_4$ electrolyte revealed earlier voltage onset of EC dehydrogenation than NMC622 charged with $LiPF_6$ electrolyte (4.1 V_{Li} with $LiBF_4$, 4.6 V_{Li} with

$LiPF_6$), NMC 811 results indicate similar onset potentials for EC dehydrogenation. The contribution of $LiM_xF_yO_z$-like species decreased with increasing potential for NMC 111, 622 and 811 (**Figure 6d-f**), suggesting surface removal of these F-containing species. The reduction of $LiM_xF_yO_z$-like species on charged NMC electrodes might expose the reactive oxide surface to the electrolyte for subsequent cycles and further degrade/oxidize the electrolyte. Moreover, the intensity of F1s collected from charged NMC622 and 811 are larger than NMC111, indicating greater reactivity towards $LiBF_4$ as the nickel content increases, which is in agreement with previous work with 1.0 M $LiPF_6$ electrolyte by Yu et al.[14] Furthermore, unlike $LiPF_6$ results from our previous work[14], there is almost no sign of formation of B-F-O species. This is due to the differences between hydrolysis of $LiPF_6$ and $LiBF_4$ salt. While the hydrolysis of $LiPF_6$ forms POF_3 species ($LiPF_6 + H_2O \rightarrow LiF+POF_3+2HF$), the hydrolysis of $LiBF_4$ does not form B-F-O species, but H_3BO_3 species instead ($LiBF_4 + H_2O \rightarrow H_3BO_3+HF+LiF$). [119]

Discussion

Carbonate dehydrogenation reactions can be suppressed (**Figure 4**) in concentrated electrolytes with lower free-carbonate activity (**Figure 1**), providing lower resistance growth (**Figure 3**) and much higher capacity retention for cycling of Ni-rich NMC electrodes (**Figure 2**). The enhanced capacity retention is not due to the formation of coatings on NMC811 in the concentrated electrolyte (**Figure 6**). The concentrated electrolyte solutions, which have lower free-carbonate activity, have higher stability against carbonate dehydrogenation. Cycling NMC811 electrodes in the 1st formation cycle in the concentrated electrolyte and replacing this with 1.0 M solution shows almost the same capacity decay as the cycling results with 1.0 M solution (**Figure S23**), and the changes in F1s spectra together with C1s and O1s spectra indicate the formation of a non-

protective EEI layer on NMC811 surfaces. Thus, we conclude that the higher capacity retention for the cycling experiment in 3.1 M $LiPF_6$ EC/EMC solution is not a result of the formation of a protective layer to passivate further decomposition, and the electrolyte used must always be concentrated to avoid parasitic decomposition reactions of the electrolyte at the electrode surface.

Intuitively, the higher stability could arise from a difference in dehydrogenation energy between free-carbonate and Li^+-bound carbonate. However, calculated bond dissociation energies for EC dehydrogenation are 2.10 eV and 2.13 eV in free-EC and Li^+-bound-EC, respectively, as computed at the DFT/B3LYP level of theory in implicit solvent, which is almost identical and cannot explain the above observations. We thus hypothesized that the higher stability of Li^+-bound carbonates is due to slower reaction kinetics at the oxide surface. The reaction profile for EC surface-mediated oxidative dehydrogenation has been computed by Østergaard *et al.* [120] on $Li_{0.5}CoO_2$ with and without the involvement of a EC chemisorbed reaction intermediate, where the carbonyl carbon forms a bond with a surface oxygen (**Figure 7**). They reported that the EC chemisorption step lowers the activation barrier compared to a direct proton transfer path, which is kinetically inhibited (0.78 eV and 1.15 eV activation energy with and without the chemisorption step).[120] Based on the requirement for the chemisorption step, which is formed after the carbonyl oxygen of EC coordinates to the metal site of oxide surface (electrophilic attack, **Figure 7**), we calculated the interaction energy between EC and the metal site of $LiMO_2$ (M=Mn, Co, Ni), Mn-doped $LiNiO_2$ and Co-doped $LiNiO_2$, as well as EC and Li^+ ion in the electrolyte solution (ion-dipole interaction) as shown in **Table S8**. The interaction energy between EC and the oxide surface was found to be -0.5 eV or weaker, while the interaction energy of EC and Li^+ (computed in vacuum) ranges from -2.37 eV for Li^+EC to -0.78 eV for $Li^+(EC)_3$, which indicates that EC preferentially interacts with Li^+ in the solution. This result can be understood intuitively, as the

EC-Li^+ interaction is an ion-dipole interaction while the EC-oxide interaction is a dipole-dipole interaction, which is generally weaker. Therefore, if there are free-carbonate species in the electrolyte solution, this free-carbonate can interact with the oxide surface and form chemisorbed EC with a lower activation barrier for the dehydrogenation reaction. On the other hand, if the activity of free-carbonate is quite low such as the case where a dissociative salt was used in the highly concentrated region, Li^+-bound-carbonate preferentially interacts with Li^+ than with the oxide surface, making carbonate dehydrogenation more difficult. The thermodynamic reaction profile for $Li(EC)_3$ on $LiNiO_2$ with and without EC chemisorbed reaction intermediate, is reported in **Figure 7a**. We can see that the pathway involving the chemisorbed intermediate requires the desolvation of EC, which has an energy penalty of more than 1 eV. The proton transfer in the direct dehydrogenation pathway is thermodynamically uphill, and can be kinetically hindered, [120] making the oxidative dehydrogenation of EC in $Li(EC)_3$ more difficult compared to free EC, where the reaction profile for both pathways is thermodynamically flat or downhill (**Figure 7b**). Notably, the dehydrogenated states, where dehydrogenated EC is adsorbed on the surface with and without the ring opening, is less thermodynamically stable for $Li(EC)_3$ compared to free EC, due to the stability of EC coordinated to Li in solution, indicating a much lower driving force for dehydrogenation of EC in $Li(EC)_3$. This proposed mechanism shows another electrolyte design principle to suppress parasitic reactions at the electrode-electrolyte interface via tuning the solvation structure and activity of free-solvent in the electrolyte solution.

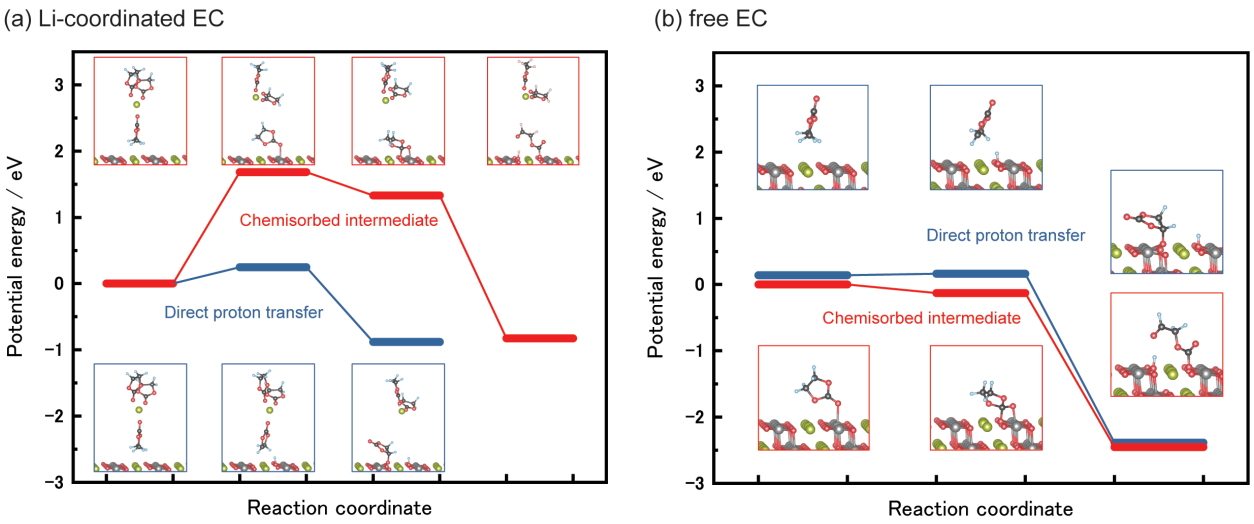

Figure 7 Computed thermodynamic potential energy diagram for surface oxidative dehydrogenation of (a) Li $(EC)_3$ complex and (b) free EC on the $(10\bar{1}4)$ surface of $LiNiO_2$, with (red line) and without (blue line) the formation of a chemisorbed reaction intermediate. The energies are referenced to the configuration where EC is bound to Li in solution for Li $(EC)_3$ and to EC with the carbonyl oxygen coordinated to the oxide metal site (electrophilic attack) for free EC. The configurations of reactants, products and reaction intermediates are shown in the insets. Li atoms are shown in light green, Ni in light gray, O in red, C in dark gray, and H in light blue. $Li^+(solvent)_3$ was identified as one of the most common solvation environments in highly concentrated solution such as 3.1 M $LiPF_6$ in EC/EMC ($LiPF_6$:EC/EMC=1:3) as supported by Raman spectroscopy shown in **Figure 1.**

Conclusions

We study the effect of electrolyte solvation structure by varying $LiPF_6$ concentration and replacing $LiPF_6$ with less dissociative $LiBF_4$ salt, on NMC111, 622 and 811 electrodes, combining battery cycling, EIS, Raman, FT-IR and XPS measurements. Solution Raman spectra show that the activity of free-carbonate species decreases either through increasing salt concentration or introducing a more dissociative salt such as $LiPF_6$ rather than $LiClO_4$ and $LiBF_4$. In particular, increasing $LiPF_6$ concentration reduced the activity of free-carbonate to the lowest value of 7 mol%

in 3.1 M $LiPF_6$ in EC:EMC (3:7wt) solution ($LiPF_6$:Carbonate = 1:3 mol/mol mixture). NMC811 electrodes cycled in highly concentrated $LiPF_6$ electrolyte exhibited higher capacity retention than electrolytes with a lower salt concentration, which is supported by less charge transfer impedance growth in the concentrated electrolyte as detected by EIS measurements. By combining Raman, DRIFT and XPS of NMC111, 622 and 811 charged in electrolytes with different $LiPF_6$ concentrations and replacing the salt with less dissociative $LiBF_4$ salt, we show evidence for earlier onset of EC dehydrogenation and the formation of protic species in the lower concentration and less dissociative electrolytes. However, by further increasing $LiPF_6$ concentration, carbonate dehydrogenation is suppressed even on the NMC811 surface. An oxide-mediated mechanism of electrolyte chemical oxidation can also be affected by solvation structure, where $LiBF_4$ has higher ionic association strength than $LiPF_6$ salt, having more free EC molecules/less Li^+ coordinated EC solvent in the electrolyte to dehydrogenate at earlier potentials. In addition, simply increasing $LiPF_6$ concentration can further suppress dehydrogenation due to much lower free-carbonate activity in the highly concentrated solution. Li^+-bound-carbonate molecules are less prone to interact with the transition-metal oxide surface, as the carbonate-Li^+ interaction is stronger than the carbonate-transition metal interaction. Therefore, it is unfavorable for carbonate species to oxidatively dehydrogenate on the oxide surface in concentrated solution which would lead to decomposition products on the NMC surface. In contrast, in less concentrated solutions where there is a considerable amount of free-carbonate species, free-carbonates can interact directly with the oxide surface, where they easily dehydrogenate. The resulting decomposition products behave as a resistor for the charge-transfer reaction, while resistance does not increase in concentrated solution, which has low free-carbonate activity. Through these findings, we propose the activity of free-carbonate as a descriptor for the chemical oxidation of EC, which provides insights into

the effect of solvation structure on electrolyte degradation in lithium ion batteries and rational design for novel salt and electrolyte. The concentrated electrolyte with lowest free-solvent activity studied in this work exhibited the highest capacity retention on NMC811 electrodes of >150 $mAhg^{-1}$ after 500 cycles upon charging to 4.6 V_{Li} (77 % capacity retention and Coulombic efficiency of 99.7 % $_{3\text{-}99th\ ave}$).

Supporting Information

Supporting Information includes 23 figures and 8 tables and can be found with this article online at xxx.

Arrhenius plots and activation energy for ionic conductivity and viscosity of electrolyte solutions (**Figure S1**), typical deconvolution example for Raman analysis (**Figure S2**),), Raman spectra for pure solvent (**Figure S3**), Raman spectra for B-F region in LiBF4 electrolyte (**Figure S4**), ATR-IR spectra for electrolytes (**Figure S5**), charge-discharge profile for 1st and 100th cycle where EIS was conducted (**Figure S6**), Cycling performance in electrolytes with different solvent (**Figure S7**), Cycling performance with lower cut-off voltage (**Figure S8**), Coulombic efficiency for charge-discharge experiments (**Figure S9**), EIS with potential holding (**Figure S10**), Electrochemical data for pellet electrodes for DRIFT (**Figure S11**), DRIFT spectra for simple mixture of salt and solvent (**Figure S12**), Raman spectra for charged pellet electrode (**Figure S13**), Capacity retention in electrolytes with different salt (**Figure S14**), NMC811 XPS for C1s and P2p region in concentrated electrolyte (**Figure S15**), Electrochemical data for carbon-free, binder-free powder electrodes for XPS with different concentration (**Figure S16**), NMC811 XPS for Li1s, Ni2p, Mn2p and Co2p region in concentrated electrolytes (**Figure S17**), NMC811, 622 and 111 XPS for C1s, B1s, Li1s, Ni2p, Mn2p and Co2p region in $LiBF_4$ electrolytes (**Figure S18**, **Figure S19**, **Figure S20**), Quantification results for XPS (**Figure S21**), Electrochemical data for carbon-free, binder-free powder electrodes for XPS with LiBF4 (**Figure S22**), Cycling performance with replacing electrolyte after formation cycle (**Figure S23**), Concentration, viscosity, density and ionic conductivity of electrolyte solutions (**Table S1**, **Table S2**, **Table S3**), XPS deconvolution parameters (**Table S4**, **Table S5**, **Table S6**, **Table S7**), calculated interaction energies (**Table S8**).

Conflicts of Interest

The authors declare no competing interests.

ACKNOWLEDGMENT

Research at MIT related to this work was supported financially by BMW. This work made use of the MRSEC Shared Experimental Facilities at MIT (XPS and SEM), supported by the National Science Foundation under award number DMR-1419807. This research used resources of the National Energy Research Scientific Computing Center, a DOE Office of Science User Facility supported by the Office of Science of the U.S. Department of Energy under Contract No. DE-AC02-05CH11231. This work also used resources of the Extreme Science and Engineering Discovery Environment (XSEDE),[121] which is supported by National Science Foundation grant number ACI-1548562. A.K.C. gratefully acknowledges the support from the Imperial-MIT Department of Materials Exchange Program.

References

(1) Noh, H.-J.; Youn, S.; Yoon, C. S.; Sun, Y.-K. Comparison of the Structural and Electrochemical Properties of Layered $Li[Ni_xCo_yMn_z]O_2$ (x= 1/3, 0.5, 0.6, 0.7, 0.8 and 0.85) Cathode Material for Lithium-Ion Batteries. *J. Power Sources* **2013**, *233*, 121–130.

(2) Hwang, S.; Kim, S. Y.; Chung, K. Y.; Stach, E. A.; Kim, S. M.; Chang, W. Determination of the Mechanism and Extent of Surface Degradation in Ni-Based Cathode Materials after Repeated Electrochemical Cycling. *APL Mater.* **2016**, *4* (9), 096105.

(3) Myung, S.-T.; Maglia, F.; Park, K.-J.; Yoon, C. S.; Lamp, P.; Kim, S.-J.; Sun, Y.-K. Nickel-Rich Layered Cathode Materials for Automotive Lithium-Ion Batteries: Achievements and Perspectives. *ACS Energy Lett.* **2016**, *2* (1), 196–223.

(4) Hwang, S.; Kim, S. M.; Bak, S.-M.; Kim, S. Y.; Cho, B.-W.; Chung, K. Y.; Lee, J. Y.; Stach, E. A.; Chang, W. Using Real-Time Electron Microscopy to Explore the Effects of Transition-Metal Composition on the Local Thermal Stability in Charged $Li_xNi_yMn_zCo_{1-y-z}O_2$ Cathode Materials. *Chem. Mater.* **2015**, *27* (11), 3927–3935.

(5) Sun, Y.-K.; Myung, S.-T.; Park, B.-C.; Prakash, J.; Belharouak, I.; Amine, K. High-Energy Cathode Material for Long-Life and Safe Lithium Batteries. *Nat. Mater.* **2009**, *8* (4), 320.

(6) Menkin, S.; Golodnitsky, D.; Peled, E. Artificial Solid-Electrolyte Interphase (SEI) for Improved Cycleability and Safety of Lithium–Ion Cells for EV Applications. *Electrochem. Commun.* **2009**, *11* (9), 1789–1791.
(7) Smith, A.; Burns, J.; Trussler, S.; Dahn, J. Precision Measurements of the Coulombic Efficiency of Lithium-Ion Batteries and of Electrode Materials for Lithium-Ion Batteries. *J. Electrochem. Soc.* **2010**, *157* (2), A196–A202.
(8) Gauthier, M.; Carney, T. J.; Grimaud, A.; Giordano, L.; Pour, N.; Chang, H.-H.; Fenning, D. P.; Lux, S. F.; Paschos, O.; Bauer, C. Electrode–Electrolyte Interface in Li-Ion Batteries: Current Understanding and New Insights. *J. Phys. Chem. Lett.* **2015**, *6* (22), 4653–4672.
(9) Jung, R.; Metzger, M.; Maglia, F.; Stinner, C.; Gasteiger, H. A. Oxygen Release and Its Effect on the Cycling Stability of $LiNi_xMn_yCo_zO_2$ (NMC) Cathode Materials for Li-Ion Batteries. *J. Electrochem. Soc.* **2017**, *164* (7), A1361–A1377.
(10) Liu, W.; Oh, P.; Liu, X.; Lee, M.; Cho, W.; Chae, S.; Kim, Y.; Cho, J. Nickel-rich Layered Lithium Transition-metal Oxide for High-energy Lithium-ion Batteries. *Angew. Chem. Int. Ed.* **2015**, *54* (15), 4440–4457.
(11) Schipper, F.; Erickson, E. M.; Erk, C.; Shin, J.-Y.; Chesneau, F. F.; Aurbach, D. Recent Advances and Remaining Challenges for Lithium Ion Battery Cathodes I. Nickel-Rich, LiNixCoyMnzO2. *J. Electrochem. Soc.* **2017**, *164* (1), A6220–A6228.
(12) Jung, R.; Metzger, M.; Maglia, F.; Stinner, C.; Gasteiger, H. A. Chemical versus Electrochemical Electrolyte Oxidation on NMC111, NMC622, NMC811, LNMO, and Conductive Carbon. *J. Phys. Chem. Lett.* **2017**, *8* (19), 4820–4825. https://doi.org/10.1021/acs.jpclett.7b01927.
(13) Xu, K. Nonaqueous Liquid Electrolytes for Lithium-Based Rechargeable Batteries. *Chem. Rev.* **2004**, *104*, 4303–4418. https://doi.org/10.1021/CR030203G.
(14) Yu, Y.; Karayaylali, P.; Katayama, Y.; Giordano, L.; Gauthier, M.; Maglia, F.; Jung, R.; Lund, I.; Shao-Horn, Y. Coupled LiPF6 Decomposition and Carbonate Dehydrogenation Enhanced by Highly Covalent Metal Oxides in High-Energy Li-Ion Batteries. *J. Phys. Chem. C* **2018**, *122* (48), 27368–27382.
(15) Jung, R.; Morasch, R.; Karayaylali, P.; Phillips, K.; Maglia, F.; Stinner, C.; Shao-Horn, Y.; Gasteiger, H. A. Effect of Ambient Storage on the Degradation of Ni-Rich Positive Electrode Materials (NMC811) for Li-Ion Batteries. *J. Electrochem. Soc.* **2018**, *165* (2), A132–A141.
(16) Giordano, L.; Karayaylali, P.; Yu, Y.; Katayama, Y.; Maglia, F.; Lux, S.; Shao-Horn, Y. Chemical Reactivity Descriptor for the Oxide-Electrolyte Interface in Li-Ion Batteries. *J. Phys. Chem. Lett.* **2017**, *8* (16), 3881–3887.
(17) Gauthier, M.; Karayaylali, P.; Giordano, L.; Feng, S.; Lux, S. F.; Maglia, F.; Lamp, P.; Shao-Horn, Y. Probing Surface Chemistry Changes Using $LiCoO_2$-Only Electrodes in Li-Ion Batteries. *J. Electrochem. Soc.* **2018**, *165* (7), A1377–A1387. https://doi.org/10.1149/2.0431807jes.
(18) Wandt, J.; Freiberg, A. T.; Ogrodnik, A.; Gasteiger, H. A. Singlet Oxygen Evolution from Layered Transition Metal Oxide Cathode Materials and Its Implications for Lithium-Ion Batteries. *Mater. Today* **2018**, *21*, 825–833.
(19) Goodenough, J. B.; Kim, Y. Challenges for Rechargeable Li Batteries. *Chem. Mater.* **2009**, *22* (3), 587–603.

(20) Grimaud, A.; Diaz-Morales, O.; Han, B.; Hong, W. T.; Lee, Y.-L.; Giordano, L.; Stoerzinger, K. A.; Koper, M. T.; Shao-Horn, Y. Activating Lattice Oxygen Redox Reactions in Metal Oxides to Catalyse Oxygen Evolution. *Nat. Chem.* **2017**, *9* (5), 457.
(21) Tarascon, J.; Vaughan, G.; Chabre, Y.; Seguin, L.; Anne, M.; Strobel, P.; Amatucci, G. In Situ Structural and Electrochemical Study of $Ni_{1-x}Co_xO_2$ Metastable Oxides Prepared by Soft Chemistry. *J. Solid State Chem.* **1999**, *147* (1), 410–420.
(22) Rivadulla, F.; Zhou, J.-S.; Goodenough, J. Chemical, Structural, and Transport Properties of Na 1− x CoO 2. *Phys. Rev. B* **2003**, *68* (7), 075108.
(23) Aydinol, M. K.; Kohan, A. F.; Ceder, G.; Cho, K.; Joannopoulos, J. Ab Initio Study of Lithium Intercalation in Metal Oxides and Metal Dichalcogenides. *Phys. Rev. B* **1997**, *56* (3), 1354.
(24) Leung, K. First-Principles Modeling of the Initial Stages of Organic Solvent Decomposition on Li x Mn2O4 (100) Surfaces. *J. Phys. Chem. C* **2012**, *116* (18), 9852–9861.
(25) Giordano, L.; Østergaard, T. M.; Muy, S.; Yu, Y.; Charles, N.; Kim, S.; Zhang, Y.; Maglia, F.; Jung, R.; Lund, I.; et al. Ligand-Dependent Energetics for Dehydrogenation: Implications in Li-Ion Battery Electrolyte Stability and Selective Oxidation Catalysis of Hydrogen-Containing Molecules. *Chem. Mater.* **2019**, *31* (15), 5464–5474. https://doi.org/10.1021/acs.chemmater.9b00767.
(26) Guéguen, A.; Streich, D.; He, M.; Mendez, M.; Chesneau, F. F.; Novák, P.; Berg, E. J. Decomposition of $LiPF_6$ in High Energy Lithium-Ion Batteries Studied with Online Electrochemical Mass Spectrometry. *J. Electrochem. Soc.* **2016**, *163* (6), A1095–A1100.
(27) Terborg, L.; Nowak, S.; Passerini, S.; Winter, M.; Karst, U.; Haddad, P. R.; Nesterenko, P. N. Ion Chromatographic Determination of Hydrolysis Products of Hexafluorophosphate Salts in Aqueous Solution. *Anal. Chim. Acta* **2012**, *714*, 121–126.
(28) Han, B.; Paulauskas, T.; Key, B.; Peebles, C.; Park, J. S.; Klie, R. F.; Vaughey, J. T.; Dogan, F. Understanding the Role of Temperature and Cathode Composition on Interface and Bulk: Optimizing Aluminum Oxide Coatings for Li-Ion Cathodes. *ACS Appl. Mater. Interfaces* **2017**, *9* (17), 14769–14778.
(29) Wise, A. M.; Ban, C.; Weker, J. N.; Misra, S.; Cavanagh, A. S.; Wu, Z.; Li, Z.; Whittingham, M. S.; Xu, K.; George, S. M. Effect of Al_2O_3 Coating on Stabilizing $LiNi_{0.4}Mn_{0.4}Co_{0.2}O_2$ Cathodes. *Chem. Mater.* **2015**, *27* (17), 6146–6154.
(30) Cho, J.; Kim, T.-G.; Kim, C.; Lee, J.-G.; Kim, Y.-W.; Park, B. Comparison of Al_2O_3-and $AlPO_4$-Coated $LiCoO_2$ Cathode Materials for a Li-Ion Cell. *J. Power Sources* **2005**, *146* (1–2), 58–64.
(31) Zhang, X.; Belharouak, I.; Li, L.; Lei, Y.; Elam, J. W.; Nie, A.; Chen, X.; Yassar, R. S.; Axelbaum, R. L. Structural and Electrochemical Study of Al_2O_3 and TiO_2 Coated $Li_{1.2}Ni_{0.13}Mn_{0.54}Co_{0.13}O_2$ Cathode Material Using ALD. *Adv. Energy Mater.* **2013**, *3* (10), 1299–1307.
(32) Cheng, H.-M.; Wang, F.-M.; Chu, J. P.; Santhanam, R.; Rick, J.; Lo, S.-C. Enhanced Cycleabity in Lithium Ion Batteries: Resulting from Atomic Layer Depostion of Al_2O_3 or TiO_2 on $LiCoO_2$ Electrodes. *J. Phys. Chem. C* **2012**, *116* (14), 7629–7637.
(33) Sun, Y.-K.; Lee, B.-R.; Noh, H.-J.; Wu, H.; Myung, S.-T.; Amine, K. A Novel Concentration-Gradient Li $[Ni_{0.83}Co_{0.07}Mn_{0.10}]O_2$ Cathode Material for High-Energy Lithium-Ion Batteries. *J. Mater. Chem.* **2011**, *21* (27), 10108–10112.

(34) Hua, C.; Du, K.; Tan, C.; Peng, Z.; Cao, Y.; Hu, G. Study of Full Concentration-Gradient Li($Ni_{0.8}Co_{0.1}Mn_{0.1}$)O_2 Cathode Material for Lithium Ion Batteries. *J. Alloys Compd.* **2014**, *614*, 264–270.
(35) Yoon, C. S.; Kim, S. J.; Kim, U.-H.; Park, K.-J.; Ryu, H.-H.; Kim, H.-S.; Sun, Y.-K. Microstructure Evolution of Concentration Gradient Li [$Ni_{0.75}Co_{0.10}Mn_{0.15}$]$O_2$ Cathode for Lithium-Ion Batteries. *Adv. Funct. Mater.* **2018**, *28*, 1802090.
(36) Sun, Y.-K.; Kim, D.-H.; Jung, H.-G.; Myung, S.-T.; Amine, K. High-Voltage Performance of Concentration-Gradient Li [$Ni_{0.67}Co_{0.15}Mn_{0.18}$]$O_2$ Cathode Material for Lithium-Ion Batteries. *Electrochimica Acta* **2010**, *55* (28), 8621–8627.
(37) Karayaylali, P.; Tatara, R.; Zhang, Y.; Chan, K.-L.; Yu, Y.; Giordano, L.; Maglia, F.; Jung, R.; Lund, I.; Shao-Horn, Y. Coating-Dependent Electrode-Electrolyte Interface for Ni-Rich Positive Electrodes in Li-Ion Batteries. *J. Electrochem. Soc.* **2019**, *166* (6), A1022–A1030. https://doi.org/10.1149/2.0461906jes.
(38) Haregewoin, A. M.; Wotango, A. S.; Hwang, B.-J. Electrolyte Additives for Lithium Ion Battery Electrodes: Progress and Perspectives. *Energy Environ. Sci.* **2016**, *9* (6), 1955–1988.
(39) Kim, G.-Y.; Dahn, J. The Effect of Some Nitriles as Electrolyte Additives in Li-Ion Batteries. *J. Electrochem. Soc.* **2015**, *162* (3), A437–A447.
(40) Petibon, R.; Rotermund, L.; Dahn, J. Evaluation of Phenyl Carbonates as Electrolyte Additives in Lithium-Ion Batteries. *J. Power Sources* **2015**, *287*, 184–195.
(41) Ma, L.; Ellis, L.; Glazier, S. L.; Ma, X.; Dahn, J. R. Combinations of $LiPO_2F_2$ and Other Electrolyte Additives in Li [$Ni_{0.5}Mn_{0.3}Co_{0.2}$]O_2/Graphite Pouch Cells. *J. Electrochem. Soc.* **2018**, *165* (9), A1718–A1724.
(42) Li, J.; Liu, H.; Xia, J.; Cameron, A. R.; Nie, M.; Botton, G. A.; Dahn, J. The Impact of Electrolyte Additives and Upper Cut-off Voltage on the Formation of a Rocksalt Surface Layer in $LiNi_{0.8}Mn_{0.1}Co_{0.1}O_2$ Electrodes. *J. Electrochem. Soc.* **2017**, *164* (4), A655–A665.
(43) Xu, C.; Renault, S.; Ebadi, M.; Wang, Z.; Björklund, E.; Guyomard, D.; Brandell, D.; Edström, K.; Gustafsson, T. LiTDI: A Highly Efficient Additive for Electrolyte Stabilization in Lithium-Ion Batteries. *Chem. Mater.* **2017**, *29* (5), 2254–2263.
(44) Cao, Z.; Hashinokuchi, M.; Doi, T.; Inaba, M. Improved Cycle Performance of $LiNi_{0.8}Co_{0.1}Mn_{0.1}O_2$ Positive Electrode Material in Highly Concentrated $LiBF_4$/DMC. *J. Electrochem. Soc.* **2019**, *166* (2), A82–A88. https://doi.org/10.1149/2.0291902jes.
(44) Doi, T.; Hashinokuchi, M.; Inaba, M. Solvation-Controlled Ester-Based Concentrated Electrolyte Solutions for High-Voltage Lithium-Ion Batteries. *Curr. Opin. Electrochem.* **2018**, *9*, 49–55.
(46) Doi, T.; Masuhara, R.; Hashinokuchi, M.; Shimizu, Y.; Inaba, M. Concentrated LiPF6/PC Electrolyte Solutions for 5-V $LiNi_{0.5}Mn_{1.5}O_4$ Positive Electrode in Lithium-Ion Batteries. *Electrochimica Acta* **2016**, *209*, 219–224. https://doi.org/10.1016/j.electacta.2016.05.062.
(47) Doi, T.; Shimizu, Y.; Hashinokuchi, M.; Inaba, M. Dilution of Highly Concentrated $LiBF_4$ /Propylene Carbonate Electrolyte Solution with Fluoroalkyl Ethers for 5-V $LiNi_{0.5}Mn_{1.5}O_4$ Positive Electrodes. *J. Electrochem. Soc.* **2017**, *164* (1), A6412–A6416. https://doi.org/10.1149/2.0611701jes.
(48) Doi, T.; Shimizu, Y.; Hashinokuchi, M.; Inaba, M. LiBF4-Based Concentrated Electrolyte Solutions for Suppression of Electrolyte Decomposition and Rapid Lithium-

Ion Transfer at $LiNi_{0.5}Mn_{1.5}O_4$/Electrolyte Interface. *J. Electrochem. Soc.* **2016**, *163* (10), A2211–A2215. https://doi.org/10.1149/2.0331610jes.
(49) Doi, T.; Shimizu, Y.; Matsumoto, R.; Hashinokuchi, M.; Inaba, M. Suppression of Mn-Ion-Dissolution of $LiNi_{0.5}Mn_{1.5}O_4$ Electrodes in a Highly Concentrated Electrolyte Solution at Elevated Temperatures. *ChemistrySelect* **2017**, *2* (28), 8824–8827. https://doi.org/10.1002/slct.201701668.
(50) Shakourian-Fard, M.; Kamath, G.; Sankaranarayanan, S. K. Evaluating the Free Energies of Solvation and Electronic Structures of Lithium-Ion Battery Electrolytes. *ChemPhysChem* **2016**, *17* (18), 2916–2930.
(51) Chen, R.; Wu, F.; Li, L.; Qiu, X.; Chen, L.; Chen, S. The Structure–Activity Relationship Studies of Binary Room Temperature Complex Electrolytes Based on LiTFSI and Organic Compounds with Acylamino Group. *Vib. Spectrosc.* **2007**, *44* (2), 297–307.
(52) Chen, R.; Wu, F.; Li, L.; Xu, B.; Qiu, X.; Chen, S. Novel Binary Room-Temperature Complex System Based on LiTFSI and 2-Oxazolidinone and Its Characterization as Electrolyte. *J. Phys. Chem. C* **2007**, *111* (13), 5184–5194.
(53) Han, S.-D.; Yun, S.-H.; Borodin, O.; Seo, D. M.; Sommer, R. D.; Young Jr, V. G.; Henderson, W. A. Solvate Structures and Computational/Spectroscopic Characterization of $LiPF_6$ Electrolytes. *J. Phys. Chem. C* **2015**, *119* (16), 8492–8500.
(54) Tamura, T.; Yoshida, K.; Hachida, T.; Tsuchiya, M.; Nakamura, M.; Kazue, Y.; Tachikawa, N.; Dokko, K.; Watanabe, M. Physicochemical Properties of Glyme–Li Salt Complexes as a New Family of Room-Temperature Ionic Liquids. *Chem. Lett.* **2010**, *39* (7), 753–755.
(55) Yoshida, K.; Nakamura, M.; Kazue, Y.; Tachikawa, N.; Tsuzuki, S.; Seki, S.; Dokko, K.; Watanabe, M. Oxidative-Stability Enhancement and Charge Transport Mechanism in Glyme-Lithium Salt Equimolar Complexes. *J Am Chem Soc* **2011**, *133* (33), 13121–13129. https://doi.org/10.1021/ja203983r.
(56) Doi, T.; Shimizu, Y.; Hashinokuchi, M.; Inaba, M. LiBF4-Based Concentrated Electrolyte Solutions for Suppression of Electrolyte Decomposition and Rapid Lithium-Ion Transfer at $LiNi_{0.5}Mn_{1.5}O_4$/Electrolyte Interface. *J. Electrochem. Soc.* **2016**, *163* (10), A2211–A2215.
(57) Wang, J.; Yamada, Y.; Sodeyama, K.; Chiang, C. H.; Tateyama, Y.; Yamada, A. Superconcentrated Electrolytes for a High-Voltage Lithium-Ion Battery. *Nat Commun* **2016**, *7*, 12032. https://doi.org/10.1038/ncomms12032.
(58) Tatara, R.; Karayaylali, P.; Yu, Y.; Zhang, Y.; Giordano, L.; Maglia, F.; Jung, R.; Schmidt, J. P.; Lund, I.; Shao-Horn, Y. The Effect of Electrode-Electrolyte Interface on the Electrochemical Impedance Spectra for Positive Electrode in Li-Ion Battery. *J. Electrochem. Soc.* **2018**, *166* (3), A5090–A5098. https://doi.org/10.1149/2.0121903jes.
(59) Tamura, T.; Yoshida, K.; Hachida, T.; Tsuchiya, M.; Nakamura, M.; Kazue, Y.; Tachikawa, N.; Dokko, K.; Watanabe, M. Physicochemical Properties of Glyme–Li Salt Complexes as a New Family of Room-Temperature Ionic Liquids. *Chem. Lett.* **2010**, *39* (7), 753–755. https://doi.org/10.1246/cl.2010.753.
(60) Yoshida, K.; Tsuchiya, M.; Tachikawa, N.; Dokko, K.; Watanabe, M. Change from Glyme Solutions to Quasi-Ionic Liquids for Binary Mixtures Consisting of Lithium Bis(Trifluoromethanesulfonyl)Amide and Glymes. *J. Phys. Chem. C* **2011**, *115* (37), 18384–18394. https://doi.org/10.1021/jp206881t.

(61) Terada, S.; Mandai, T.; Nozawa, R.; Yoshida, K.; Ueno, K.; Tsuzuki, S.; Dokko, K.; Watanabe, M. Physicochemical Properties of Pentaglyme-Sodium Bis(Trifluoromethanesulfonyl)Amide Solvate Ionic Liquid. *Phys Chem Chem Phys* **2014**, *16* (23), 11737–11746. https://doi.org/10.1039/c4cp00746h.
(62) Mandai, T.; Yoshida, K.; Ueno, K.; Dokko, K.; Watanabe, M. Criteria for Solvate Ionic Liquids. *Phys Chem Chem Phys* **2014**, *16* (19), 8761–8772. https://doi.org/10.1039/c4cp00461b.
(62) Watanabe, M.; Thomas, M. L.; Zhang, S.; Ueno, K.; Yasuda, T.; Dokko, K. Application of Ionic Liquids to Energy Storage and Conversion Materials and Devices. *Chem. Rev.* **2017**, *117*, 7190–7239.
(64) Shigenobu, K.; Nakanishi, A.; Ueno, K.; Dokko, K.; Watanabe, M. Glyme–Li Salt Equimolar Molten Solvates with Iodide/Triiodide Redox Anions. *RSC Adv.* **2019**, *9* (39), 22668–22675. https://doi.org/10.1039/C9RA03580J.
(65) Tamura, T.; Hachida, T.; Yoshida, K.; Tachikawa, N.; Dokko, K.; Watanabe, M. New Glyme–Cyclic Imide Lithium Salt Complexes as Thermally Stable Electrolytes for Lithium Batteries. *J. Power Sources* **2010**, *195* (18), 6095–6100. https://doi.org/10.1016/j.jpowsour.2009.11.061.
(66) Suo, L.; Borodin, O.; Gao, T.; Olguin, M.; Ho, J.; Fan, X.; Luo, C.; Wang, C.; Xu, K. "Water-in-Salt" Electrolyte Enables High-Voltage Aqueous Lithium-Ion Chemistries. *Science* **2015**, *350* (6263), 938–943. https://doi.org/10.1126/science.aab1595.
(67) Wang, J.; Yamada, Y.; Sodeyama, K.; Chiang, C. H.; Tateyama, Y.; Yamada, A. Superconcentrated Electrolytes for a High-Voltage Lithium-Ion Battery. *Nat. Commun.* **2016**, *7*, 12032.
(68) Yamada, Y.; Furukawa, K.; Sodeyama, K.; Kikuchi, K.; Yaegashi, M.; Tateyama, Y.; Yamada, A. Unusual Stability of Acetonitrile-Based Superconcentrated Electrolytes for Fast-Charging Lithium-Ion Batteries. *J Am Chem Soc* **2014**, *136* (13), 5039–5046. https://doi.org/10.1021/ja412807w.
(69) Huang, M.; Feng, S.; Zhang, W.; Lopez, J.; Qiao, B.; Tatara, R.; Giordano, L.; Shao-Horn, Y.; Johnson, J. A. Design of S-Substituted Fluorinated Aryl Sulfonamide Tagged (S-FAST) Anions to Enable New Solvate Ionic Liquids for Battery Applications. *Chem. Mater.* **2019**, *in press*. https://doi.org/10.1021/acs.chemmater.9b02353.
(70) Dokko, K.; Watanabe, D.; Ugata, Y.; Thomas, M. L.; Tsuzuki, S.; Shinoda, W.; Hashimoto, K.; Ueno, K.; Umebayashi, Y.; Watanabe, M. Direct Evidence for Li Ion Hopping Conduction in Highly Concentrated Sulfolane-Based Liquid Electrolytes. *J Phys Chem B* **2018**, *122* (47), 10736–10745. https://doi.org/10.1021/acs.jpcb.8b09439.
(71) Nakanishi, A.; Ueno, K.; Watanabe, D.; Ugata, Y.; Matsumae, Y.; Liu, J.; Thomas, M. L.; Dokko, K.; Watanabe, M. Sulfolane-Based Highly Concentrated Electrolytes of Lithium Bis(Trifluoromethanesulfonyl)Amide: Ionic Transport, Li-Ion Coordination, and Li–S Battery Performance. *J. Phys. Chem. C* **2019**, *123* (23), 14229–14238. https://doi.org/10.1021/acs.jpcc.9b02625.
(72) Ugata, Y.; Thomas, M. L.; Mandai, T.; Ueno, K.; Dokko, K.; Watanabe, M. Li-Ion Hopping Conduction in Highly Concentrated Lithium Bis(Fluorosulfonyl)Amide/Dinitrile Liquid Electrolytes. *Phys. Chem. Chem. Phys.* **2019**, *21* (19), 9759–9768. https://doi.org/10.1039/C9CP01839E.
(73) Abe, T.; Kawabata, N.; Mizutani, Y.; Inaba, M.; Ogumi, Z. Correlation Between Cointercalation of Solvents and Electrochemical Intercalation of Lithium into Graphite in

Propylene Carbonate Solution. *J. Electrochem. Soc.* **2003**, *150* (3), A257. https://doi.org/10.1149/1.1541004.
(74) Yamada, Y.; Yamada, A. Review—Superconcentrated Electrolytes for Lithium Batteries. *J. Electrochem. Soc.* **2015**, *162* (14), A2406–A2423. https://doi.org/10.1149/2.0041514jes.
(75) Tatara, R.; Kwabi, D. G.; Batcho, T. P.; Tulodziecki, M.; Watanabe, K.; Kwon, H.-M.; Thomas, M. L.; Ueno, K.; Thompson, C. V.; Dokko, K.; et al. Oxygen Reduction Reaction in Highly Concentrated Electrolyte Solutions of Lithium Bis(Trifluoromethanesulfonyl)Amide/Dimethyl Sulfoxide. *J. Phys. Chem. C* **2017**. https://doi.org/10.1021/acs.jpcc.7b01738.
(76) Terada, S.; Susa, H.; Tsuzuki, S.; Mandai, T.; Ueno, K.; Dokko, K.; Watanabe, M. Glyme-Sodium Bis(Fluorosulfonyl)Amide Complex Electrolytes for Sodium Ion Batteries. *J. Phys. Chem. C* **2018**. https://doi.org/10.1021/acs.jpcc.8b04367.
(77) Chan, A. K.; Tatara, R.; Feng, S.; Karayaylali, P.; Lopez, J.; Stephens, I. E. L.; Shao-Horn, Y. Concentrated Electrolytes for Enhanced Stability of Al-Alloy Negative Electrodes in Li-Ion Batteries. *J. Electrochem. Soc.* **2019**, *166* (10), A1867–A1874. https://doi.org/10.1149/2.0581910jes.
(78) Suo, L.; Hu, Y.-S.; Li, H.; Armand, M.; Chen, L. A New Class of Solvent-in-Salt Electrolyte for High-Energy Rechargeable Metallic Lithium Batteries. *Nat. Commun.* **2013**, *4* (1), 1481. https://doi.org/10.1038/ncomms2513.
(79) Petibon, R.; Aiken, C. P.; Ma, L.; Xiong, D.; Dahn, J. R. The Use of Ethyl Acetate as a Sole Solvent in Highly Concentrated Electrolyte for Li-Ion Batteries. *Electrochimica Acta* **2015**, *154*, 287–293. https://doi.org/10.1016/j.electacta.2014.12.093.
(80) Armand, M.; Tarascon, J.-M. Building Better Batteries. *Nature* **2008**, *451*, 652–657. https://doi.org/10.1038/451652a.
(81) Ueno, K.; Tatara, R.; Tsuzuki, S.; Saito, S.; Doi, H.; Yoshida, K.; Mandai, T.; Matsugami, M.; Umebayashi, Y.; Dokko, K.; et al. Li+ Solvation in Glyme-Li Salt Solvate Ionic Liquids. *Phys Chem Chem Phys* **2015**, *17* (12), 8248–8257. https://doi.org/10.1039/c4cp05943c.
(82) Mandai, T.; Dokko, K.; Watanabe, M. Solvate Ionic Liquids for Li, Na, K, and Mg Batteries. *Chem. Rec.* **2019**, *19* (4), 708–722. https://doi.org/10.1002/tcr.201800111.
(83) Tatara, R.; Ueno, K.; Dokko, K.; Watanabe, M. Thermodynamic Effect of Anion Activity on Electrochemical Reactions Involving Li+ Ions in Room-Temperature Ionic Liquids. *ChemElectroChem* **2019**, *in press*. https://doi.org/10.1002/celc.201900973.
(84) Jeong, S.-K.; Inaba, M.; Iriyama, Y.; Abe, T.; Ogumi, Z. Electrochemical Intercalation of Lithium Ion within Graphite from Propylene Carbonate Solutions. *Electrochem. Solid-State Lett.* **2003**, *6* (1), A13. https://doi.org/10.1149/1.1526781.
(85) Heckmann, A.; Thienenkamp, J.; Beltrop, K.; Winter, M.; Brunklaus, G.; Placke, T. Towards High-Performance Dual-Graphite Batteries Using Highly Concentrated Organic Electrolytes. *Electrochimica Acta* **2018**, *260*, 514–525. https://doi.org/10.1016/j.electacta.2017.12.099.
(86) Ellis, L. D.; Xia, J.; Louli, A. J.; Dahn, J. R. Effect of Substituting $LiBF_4$ for $LiPF_6$ in High Voltage Lithium-Ion Cells Containing Electrolyte Additives. *J. Electrochem. Soc.* **2016**, *163* (8), A1686–A1692.

(87) Parimalam, B. S.; Lucht, B. L. Reduction Reactions of Electrolyte Salts for Lithium Ion Batteries: LiPF6, LiBF4, LiDFOB, LiBOB, and LiTFSI. *J. Electrochem. Soc.* **2018**, *165* (2), A251–A255.
(88) Ellis, L. D.; Hill, I. G.; Gering, K. L.; Dahn, J. R. Synergistic Effect of $LiPF_6$ and $LiBF_4$ as Electrolyte Salts in Lithium-Ion Cells. *J. Electrochem. Soc.* **2017**, *164* (12), A2426–A2433.
(89) von Wald Cresce, A.; Gobet, M.; Borodin, O.; Peng, J.; Russell, S. M.; Wikner, E.; Fu, A.; Hu, L.; Lee, H.-S.; Zhang, Z. Anion Solvation in Carbonate-Based Electrolytes. *J. Phys. Chem. C* **2015**, *119* (49), 27255–27264.
(90) Seo, D. M.; Borodin, O.; Han, S.-D.; Boyle, P. D.; Henderson, W. A. Electrolyte Solvation and Ionic Association II. Acetonitrile-Lithium Salt Mixtures: Highly Dissociated Salts. *J. Electrochem. Soc.* **2012**, *159* (9), A1489–A1500.
(91) Ender, M.; Illig, J.; Ivers-Tiffée, E. Three-Electrode Setups for Lithium-Ion Batteries I. Fem-Simulation of Different Reference Electrode Designs and Their Implications for Half-Cell Impedance Spectra. *J. Electrochem. Soc.* **2016**, *164* (2), A71–A79. https://doi.org/10.1149/2.0231702jes.
(92) Costard, J.; Ender, M.; Weiss, M.; Ivers-Tiffée, E. Three-Electrode Setups for Lithium-Ion Batteries II. Experimental Study of Different Reference Electrode Designs and Their Implications for Half-Cell Impedance Spectra. *J. Electrochem. Soc.* **2016**, *164* (2), A80–A87. https://doi.org/10.1149/2.0241702jes.
(93) Cresce, A. V.; Russell, S. M.; Borodin, O.; Allen, J. A.; Schroeder, M. A.; Dai, M.; Peng, J.; Gobet, M. P.; Greenbaum, S. G.; Rogers, R. E.; et al. Solvation Behavior of Carbonate-Based Electrolytes in Sodium Ion Batteries. *Phys. Chem. Chem. Phys.* **2017**, *19* (1), 574–586. https://doi.org/10.1039/C6CP07215A.
(94) Frisch, M.; Trucks, G.; Schlegel, H.; Scuseria, G.; Robb, M.; Cheeseman, J.; Scalmani, G.; Barone, V.; Mennucci, B.; Petersson, G. Gaussian 09, Revision A. 02; Gaussian, Inc: Wallingford, CT, 2009. *Google Sch.* **2015**.
(95) Perdew, J. P.; Burke, K.; Ernzerhof, M. Generalized Gradient Approximation Made Simple. *Phys. Rev. Lett.* **1996**, *77* (18), 3865–3868. https://doi.org/10.1103/PhysRevLett.77.3865.
(96) Kresse, G.; Hafner, J. *Ab Initio* Molecular Dynamics for Liquid Metals. *Phys. Rev. B* **1993**, *47* (1), 558–561. https://doi.org/10.1103/PhysRevB.47.558.
(97) Kresse, G.; Furthmüller, J. Efficient Iterative Schemes for *Ab Initio* Total-Energy Calculations Using a Plane-Wave Basis Set. *Phys. Rev. B* **1996**, *54* (16), 11169–11186. https://doi.org/10.1103/PhysRevB.54.11169.
(98) Anisimov, V. I.; Aryasetiawan, F.; Lichtenstein, A. I. First-Principles Calculations of the Electronic Structure and Spectra of Strongly Correlated Systems: The **LDA** + *U* Method. *J. Phys. Condens. Matter* **1997**, *9* (4), 767–808. https://doi.org/10.1088/0953-8984/9/4/002.
(99) Dudarev, S. L.; Botton, G. A.; Savrasov, S. Y.; Humphreys, C. J.; Sutton, A. P. Electron-Energy-Loss Spectra and the Structural Stability of Nickel Oxide: An LSDA+U Study. *Phys. Rev. B* **1998**, *57* (3), 1505–1509. https://doi.org/10.1103/PhysRevB.57.1505.
(100) Wang, L.; Maxisch, T.; Ceder, G. Oxidation Energies of Transition Metal Oxides within the GGA + U Framework. *Phys. Rev. B* **2006**, *73* (19). https://doi.org/10.1103/PhysRevB.73.195107.

(101) Lee, Y.-L.; Kleis, J.; Rossmeisl, J.; Morgan, D. *Ab Initio* Energetics of $LaBO_3$ (001) (B = Mn, Fe, Co, and Ni) for Solid Oxide Fuel Cell Cathodes. *Phys. Rev. B* **2009**, *80* (22). https://doi.org/10.1103/PhysRevB.80.224101.
(102) Mukai, K.; Inoue, T.; Kato, Y.; Shirai, S. Superior Low-Temperature Power and Cycle Performances of Na-Ion Battery over Li-Ion Battery. *ACS Omega* **2017**, *2* (3), 864–872. https://doi.org/10.1021/acsomega.6b00551.
(103) Logan, E. R.; Tonita, E. M.; Gering, K. L.; Li, J.; Ma, X.; Beaulieu, L. Y.; Dahn, J. R. A Study of the Physical Properties of Li-Ion Battery Electrolytes Containing Esters. *J. Electrochem. Soc.* **2018**, *165* (2), A21–A30. https://doi.org/10.1149/2.0271802jes.
(104) Fujii, K.; Wakamatsu, H.; Todorov, Y.; Yoshimoto, N.; Morita, M. Structural and Electrochemical Properties of Li Ion Solvation Complexes in the Salt-Concentrated Electrolytes Using an Aprotic Donor Solvent, *N*,*N*-Dimethylformamide. *J. Phys. Chem. C* **2016**, *120* (31), 17196–17204. https://doi.org/10.1021/acs.jpcc.6b04542.
(105) Ueno, K.; Yoshida, K.; Tsuchiya, M.; Tachikawa, N.; Dokko, K.; Watanabe, M. Glyme–Lithium Salt Equimolar Molten Mixtures: Concentrated Solutions or Solvate Ionic Liquids? *J. Phys. Chem. B* **2012**, *116* (36), 11323–11331. https://doi.org/10.1021/jp307378j.
(106) Zhang, C.; Ueno, K.; Yamazaki, A.; Yoshida, K.; Moon, H.; Mandai, T.; Umebayashi, Y.; Dokko, K.; Watanabe, M. Chelate Effects in Glyme/Lithium Bis(Trifluoromethanesulfonyl)Amide Solvate Ionic Liquids. I. Stability of Solvate Cations and Correlation with Electrolyte Properties. *J Phys Chem B* **2014**, *118* (19), 5144–5153. https://doi.org/10.1021/jp501319e.
(107) Tatara, R.; Leverick, G. M.; Feng, S.; Wan, S.; Terada, S.; Dokko, K.; Watanabe, M.; Shao-Horn, Y. Tuning NaO_2 Cube Sizes by Controlling Na^+ and Solvent Activity in Na–O_2 Batteries. *J. Phys. Chem. C* **2018**, *122* (32), 18316–18328. https://doi.org/10.1021/acs.jpcc.8b05418.
(107) Terada, S.; Ikeda, K.; Ueno, K.; Dokko, K.; Watanabe, M. Liquid Structures and Transport Properties of Lithium Bis(Fluorosulfonyl)Amide/Glyme Solvate Ionic Liquids for Lithium Batteries. *Aust. J. Chem.* **2019**, *72*, 70–80. https://doi.org/10.1071/CH18270.
(109) Li, Z.; Zhang, S.; Zhang, C.; Ueno, K.; Yasuda, T.; Tatara, R.; Dokko, K.; Watanabe, M. One-Pot Pyrolysis of Lithium Sulfate and Graphene Nanoplatelet Aggregates: In Situ Formed Li_2S/Graphene Composite for Lithium-Sulfur Batteries. *Nanoscale* **2015**, *7* (34), 14385–14392. https://doi.org/10.1039/c5nr03201f.
(110) Jung, R.; Metzger, M.; Maglia, F.; Stinner, C.; Gasteiger, H. A. Oxygen Release and Its Effect on the Cycling Stability of $LiNi_xMn_yCo_zO_2$ (NMC) Cathode Materials for Li-Ion Batteries. *J. Electrochem. Soc.* **2017**, *164* (7), A1361–A1377. https://doi.org/10.1149/2.0021707jes.
(111) Li, X.; Liu, J.; Banis, M. N.; Lushington, A.; Li, R.; Cai, M.; Sun, X. Atomic Layer Deposition of Solid-State Electrolyte Coated Cathode Materials with Superior High-Voltage Cycling Behavior for Lithium Ion Battery Application. *Energy Env. Sci* **2014**, *7* (2), 768–778. https://doi.org/10.1039/C3EE42704H.
(112) Verdier, S.; El Ouatani, L.; Dedryvere, R.; Bonhomme, F.; Biensan, P.; Gonbeau, D. XPS Study on Al_2O_3-and $AlPO_4$-Coated $LiCoO_2$ Cathode Material for High-Capacity Li Ion Batteries. *J. Electrochem. Soc.* **2007**, *154* (12), A1088–A1099.

(113) Quinlan, R. A.; Lu, Y.-C.; Kwabi, D.; Shao-Horn, Y.; Mansour, A. N. XPS Investigation of the Electrolyte Induced Stabilization of $LiCoO_2$ and "$AlPO_4$"-Coated $LiCoO_2$ Composite Electrodes. *J. Electrochem. Soc.* **2016**, *163* (2), A300–A308.
(114) Kozlowski, C.; Sherwood, P. M. X-Ray Photoelectron-Spectroscopic Studies of Carbon-Fibre Surfaces. Part 5.—The Effect of PH on Surface Oxidation. *J. Chem. Soc. Faraday Trans. 1 Phys. Chem. Condens. Phases* **1985**, *81* (11), 2745–2756.
(115) Malmgren, S.; Ciosek, K.; Hahlin, M.; Gustafsson, T.; Gorgoi, M.; Rensmo, H.; Edström, K. Comparing Anode and Cathode Electrode/Electrolyte Interface Composition and Morphology Using Soft and Hard X-Ray Photoelectron Spectroscopy. *Electrochimica Acta* **2013**, *97*, 23–32.
(116) Dupin, J.-C.; Gonbeau, D.; Benqlilou-Moudden, H.; Vinatier, P.; Levasseur, A. XPS Analysis of New Lithium Cobalt Oxide Thin-Films before and after Lithium Deintercalation. *Thin Solid Films* **2001**, *384* (1), 23–32.
(117) Appapillai, A. T.; Mansour, A. N.; Cho, J.; Shao-Horn, Y. Microstructure of $LiCoO_2$ with and without "$AlPO_4$" Nanoparticle Coating: Combined STEM and XPS Studies. *Chem. Mater.* **2007**, *19* (23), 5748–5757.
(118) Edström, K.; Gustafsson, T.; THOMAS, J. The Cathode-Electrolyte Interface in a Li-Ion Battery. In *Lithium-ion Batteries: Solid-electrolyte Interphase*; World Scientific, 2004; pp 337–364.
(119) Parimalam, B. S.; Lucht, B. L. Reduction Reactions of Electrolyte Salts for Lithium Ion Batteries: $LiPF_6$, $LiBF_4$, LiDFOB, LiBOB, and LiTFSI. *J. Electrochem. Soc.* **2018**, *165* (2), A251–A255. https://doi.org/10.1149/2.0901802jes.
(120) Østergaard, T. M.; Giordano, L.; Castelli, I. E.; Maglia, F.; Antonopoulos, B. K.; Shao-Horn, Y.; Rossmeisl, J. Oxidation of Ethylene Carbonate on Li Metal Oxide Surfaces. *J. Phys. Chem. C* **2018**, *122* (19), 10442–10449. https://doi.org/10.1021/acs.jpcc.8b01713.
(121) Towns, J.; Cockerill, T.; Dahan, M.; Foster, I.; Gaither, K.; Grimshaw, A.; Hazlewood, V.; Lathrop, S.; Lifka, D.; Peterson, G. D.; et al. XSEDE: Accelerating Scientific Discovery. *Comput. Sci. Eng.* **2014**, *16* (5), 62–74. https://doi.org/10.1109/MCSE.2014.80.

TOC

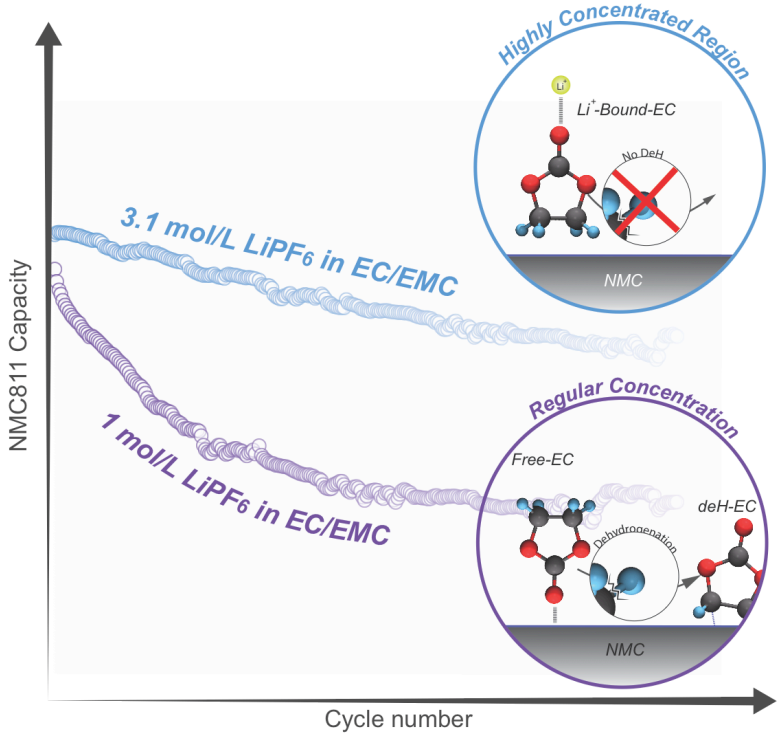
Highly Concentrated Region
Li+-Bound-EC
No DeH
NMC
3.1 mol/L LiPF6 in EC/EMC
Regular Concentration
Free-EC
deH-EC
Dehydrogenation
1 mol/L LiPF6 in EC/EMC
NMC
NMC811 Capacity
Cycle number

Supporting Information for

Enhanced Cycling Performance of Ni-rich Positive Electrodes (NMC) in Li-ion Batteries by Reducing Electrolyte Free-solvent Activity

Ryoichi Tatara†‡*[a], Yang Yu†[b], Pinar Karayaylali†[c], Averey K. Chan[b,d], Yirui Zhang[c], Roland Jung[e], Filippo Maglia[e], Livia Giordano[a, c], Yang Shao-Horn*[abc]

[a] Research Laboratory of Electronics, [b] Department of Materials Science and Engineering, [c] Department of Mechanical Engineering, Massachusetts Institute of Technology, 77 Massachusetts Ave., Cambridge, MA 02139, United States

[d] Department of Materials, Imperial College London, Royal School of Mines Building, Prince Consort Rd., London, SW7 2AZ, UK

[e] BMW Group, Petuelring 130, 80788 Munich, Germany

† Contributed equally

‡ Present address: Department of Chemistry and Biotechnology, Yokohama National University, 79-5 Tokiwadai, Hodogaya-ku, Yokohama, Kanagawa, 240-8501, Japan

* Corresponding authors (shaohorn@mit.edu, tatara-ryoichi-nx@ynu.ac.jp)

Table S 1 Molar ratio of $LiPF_6$:EC/EMC, viscosity (η), density (d), concentration of $LiPF_6$ (c) and ionic conductivity (σ) of $LiPF_6$ in EC:EMC (3:7wt) solutions at 25 °C.

$LiPF_6$:EC/EMC	[Carbonate]/[Li]	η mPa s	d g cm^{-3}	c mol dm^{-3}	σ mS cm^{-1}
1:3	3	57.0	1.37	3.06	1.98
1:4	4	20.0	1.32	2.41	4.17
1:5	5	10.7	1.27	1.97	6.45
1:8	8	4.32	1.22	1.30	9.15
1:10.5	10.5	3.00	1.19	1.00	8.88
1:25	25	1.47	1.14	0.43	6.63
1:50	50	1.22	1.12	0.22	4.15
pure EC/EMC (3:7wt)	-	0.93	1.10	0	-

Table S 2 Viscosity (η), density (d) and ionic conductivity (σ) of 1 M $LiPF_6$, $LiClO_4$ and $LiBF_4$ in EC:EMC (3:7wt) solutions at 25 °C.

1 M LiX in EC/EMC	η mPa s	d g cm^{-3}	σ mS cm^{-1}
$LiPF_6$	3.00	1.19	8.88
$LiClO_4$	2.60	1.16	5.34
$LiBF_4$	2.11	1.15	2.98
pure EC/EMC (3:7wt)	0.93	1.10	-

Table S 3 Viscosity (η), density (d) and ionic conductivity (σ) of $LiPF_6$ solution in different solvent at 25 °C. *Viscosity and density of EC was measured at supercooling liquid state at 25 °C as melting point of EC is ~35 °C. **Donor number of 16 is value for diethyl carbonate and 17.2 is value for dimethyl carbonate.

	ε_r	Donor number	η mPa s	d g cm^{-3}	σ mS cm^{-1}
1 M $LiPF_6$ in EC/EMC			3.00	1.19	8.88
1.5 M $LiPF_6$ in EC			11.00	1.44	7.19
1 M $LiPF_6$ in EMC			1.70	1.11	4.47
pure EC	90	16.4	~2.7*	1.33*	-
pure EMC	3.0	16-17.2**	0.62	1.01	-
pure EC/EMC (3:7wt)			0.93	1.10	-

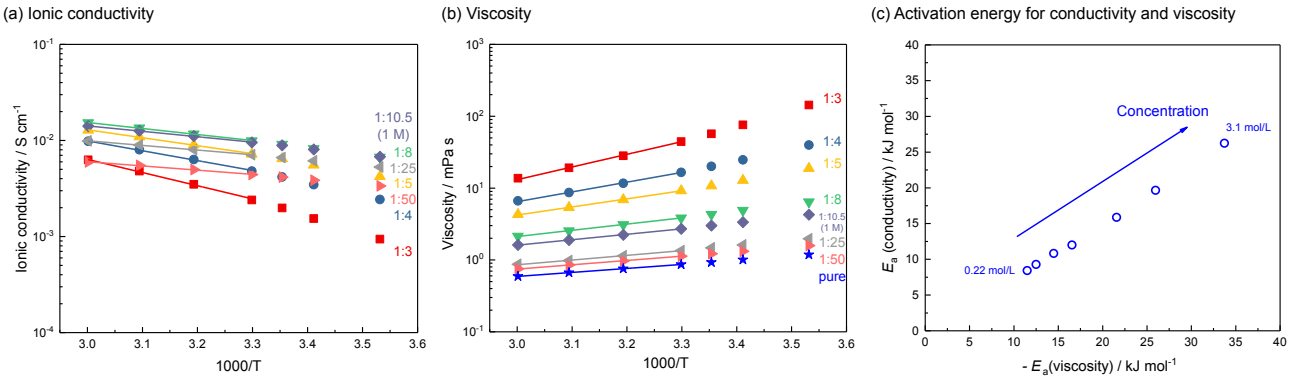

Figure S 1 Arrhenius plots for (a) ionic conductivity and (b) viscosity for various concentration range of $LiPF_6$ in EC:EMC (3:7wt) solution. To avoid the effect of glass transition, the plot was fitted only high temperature region since ionic conduction in solution electrolyte is generally governed by Vogel-Tammann-Fulcher (VTF) equation: $R^{-1} = A\exp(-E_a/R(T-T_0))$, which is glass transition temperature corrected (T_0: Vogel temperature, glass transition in ideal glasses) Arrhenius relationship, and gives straight line only at high temperature region.[1] Calculated activation energy was shown in (c), which shows linear relationship between ionic conduction and viscosity.

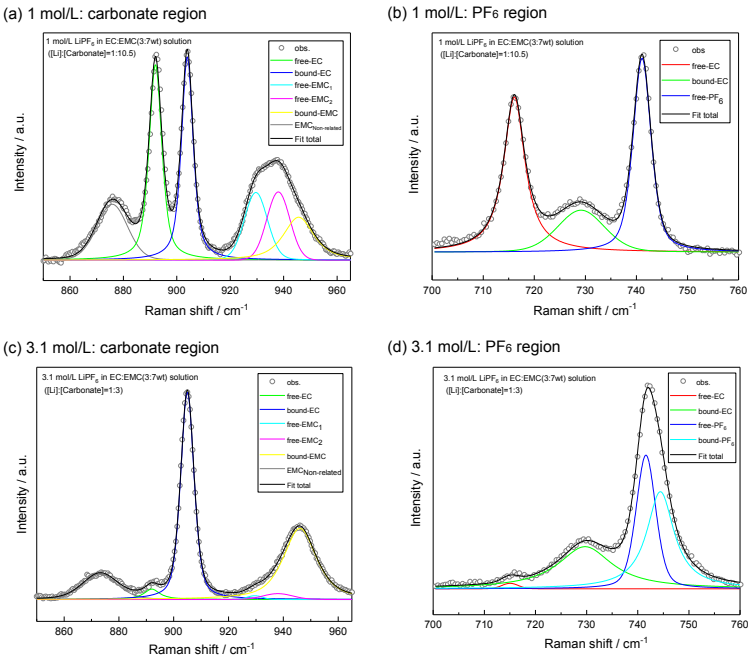

Figure S 2 Typical results on the deconvolutions of Raman spectra by the Gaussian-Lorentzian function. (a) 850 -965 cm^{-1} (carbonate bands), (b) 700-760 cm^{-1} (PF_6^- bands) regions for 1.0 M $LiPF_6$ in EC:EMC (3:7wt) solution and (c) 850 -965 cm^{-1} (carbonate bands), (d) 700-760 cm^{-1} (PF_6^- bands) regions for 3.1 M $LiPF_6$ in EC:EMC (3:7wt) solution. The spectra for 780-900 cm^{-1} were deconvoluted into 6 bands (~875, 892, ~904, ~929.6, 938 and ~946 cm^{-1}) and that for 710-780 cm^{-1} were deconvoluted into 4 bands (~716, ~729, ~741.5, ~744.4 cm^{-1}).

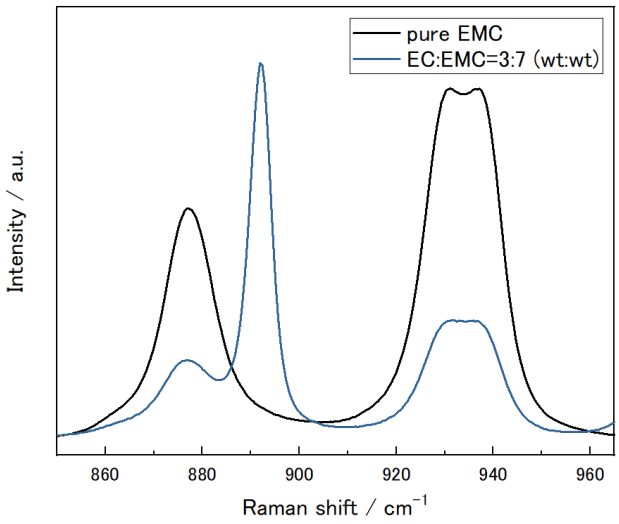

Figure S 3 Raman spectra of pure EMC and EC:EMC (3:7 wt:wt) mixtures measured at 25 °C.

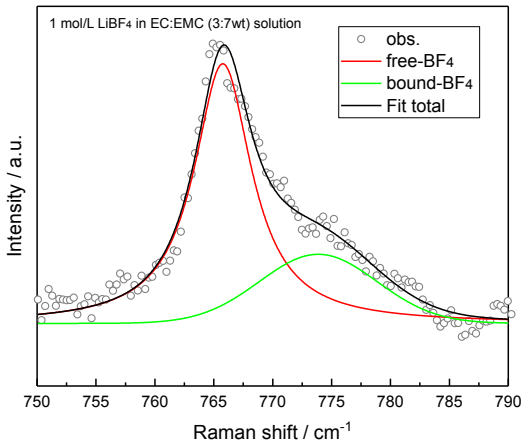

Figure S 4 Raman spectra of 1.0 M $LiBF_4$ in EC:EMC (3:7wt) solution in the B-F stretching range from 750 to 790 cm^{-1} measured at 25 °C, with 632 nm laser to suppress fluorescence effect to avoid overlapping relatively weak B-F stretching signal. The band at 765.8 cm^{-1} can be assigned to free-BF_4 and at 773.9 cm^{-1} to bound-BF_4 to Li^+ in the solution. Estimated molar fractions of Li^+-bound BF_4^- ($I_{\text{bound-BF4}}$ / $I_{\text{total-BF4}}$) in the solution based on the ratio of integral intensities is 26 %. The R^2 values for deconvolution are higher than 0.971.

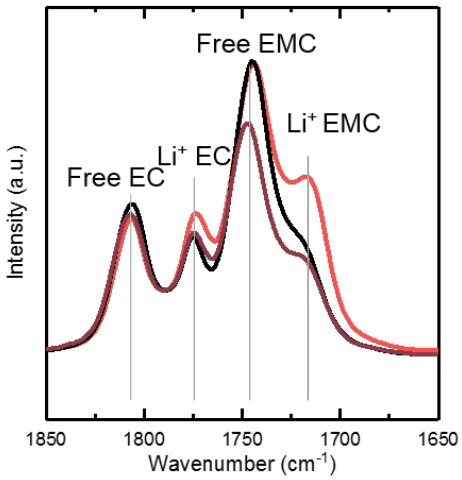

Figure S 5 Attenuated total reflection (ATR) spectra of 1.0 M $LiPF_6$ (red), $LiClO_4$ (brown) and $LiBF_4$ (black) in EC/EMC (3:7 wt:wt). The bands at 1774 and 1807 cm^{-1} represent the C=O stretching mode of EC molecule with and without Li coordination, and the bands located at 1720 cm^{-1} and 1744 cm^{-1} represent the C=O stretching of EMC molecule.

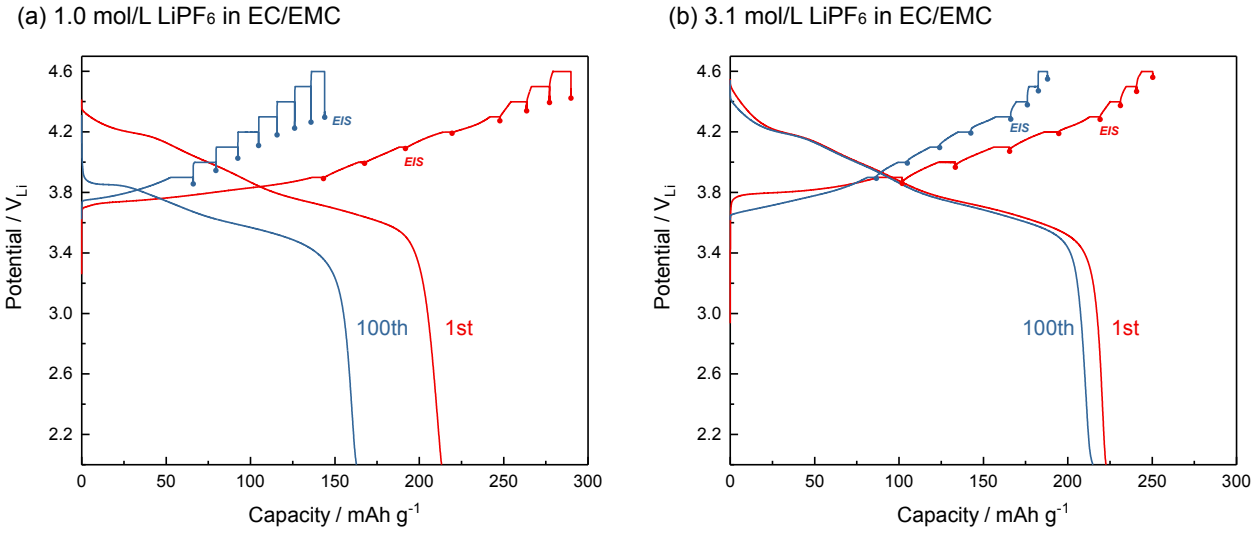

Figure S 6 Charge-discharge profile with (a) 1.0 M $LiPF_6$ and (b) 3.1 M $LiPF_6$ in EC/EMC in EC/EMC at 1st and 100th cycle conducted with 0.1C condition, while 2nd – 99th cycles were conducted at CC-CV 1C-0.05C condition. The cells were charged at 0.1C and potential was held at 3.9, 4.0, 4.1, 4.2, 4.3, 4.4, 4.5 and 4.6 V_{Li} for 1 hour, and rest 1hour followed by EIS measurement (the dots in the figure are the points EIS measurement were conducted). Slightly larger discharge capacity at 100^{th} cycle compared with the charge capacity is most likely come from residual charge from faster cycling before 99^{th} cycle.

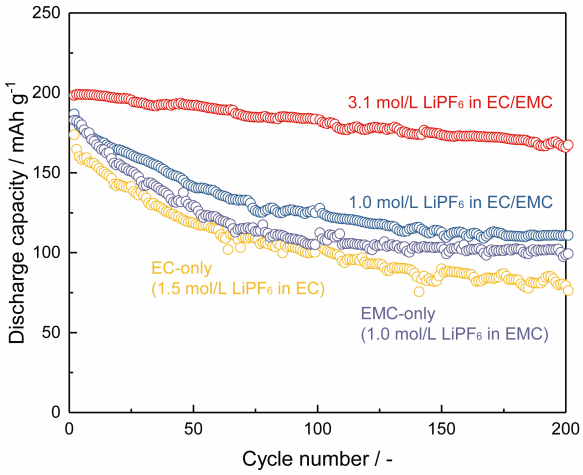

Figure S 7 Cycling performance of NMC811 composite electrodes with different electrolyte solutions upon charging to 4.6 V_{Li} (2nd-99th cycle at CC-CV 1C-0.05C condition). At the 1st and 100th cycle, the cells were measured in a three-electrode configuration, which composed of NMC811|$Li_4Ti_5O_{12}$-mesh|Li (see experimental section in detail), galvanostatically charged at 27.5 mA/g (0.1C). From the 2nd to the 99th cycle and after 101st cycle, the cells were tested with a two-electrode configuration that consisted NMC811 as the working electrode and Li metal as the counter electrode upon cycling between 4.6 and 2.0 V_{Li}. Slightly lower capacity on the EC-only and EMC-only electrolyte than EC/EMC electrolyte can be attributed to the lower ionic conductivity of EC-only and EMC-only electrolyte compared with an EC/EMC mixture electrolyte (**Table S 3**).

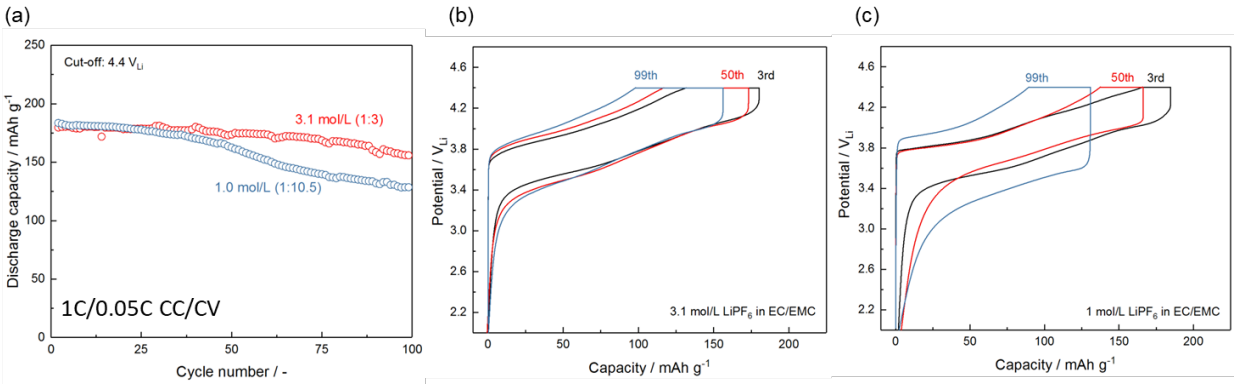

Figure S 8 Charge-discharge cycle performance of NMC811 composite electrodes with different electrolyte solutions at cut-off voltage of 4.4 V_{Li}. (a) Concentration dependent capacity retention (2nd-99th cycle at CC-CV 1C-0.05C condition) and charge-discharge profile with (b) 3.1 M $LiPF_6$ in EC/EMC and (c) 1.0 M $LiPF_6$ in EC/EMC. NMC811|$Li_4Ti_5O_{12}$-mesh|Li three electrode cell was used. At 1st and 100th cycle, the cells were operated with three-electrode configuration and galvanostatically charged at 27.5 mA/g (0.1C) with measuring EIS. From 2nd to 99th cycle and after 101st cycle, the cells were operated with two-electrode configuration (NMC811 as working electrode and Li metal as reference/counter electrode) and cycle between 4.4 and 2.0 V_{Li} with constant current – constant voltage (CCCV) condition (1C charge to 4.4 V_{Li} and hold at 4.4 V_{Li} until the current reach to 0.05C, then discharge at 1C to 2.0 V_{Li}). Only fast cycle at 1C/0.05C (CC/CV) from 2nd to 99th cycles were shown.

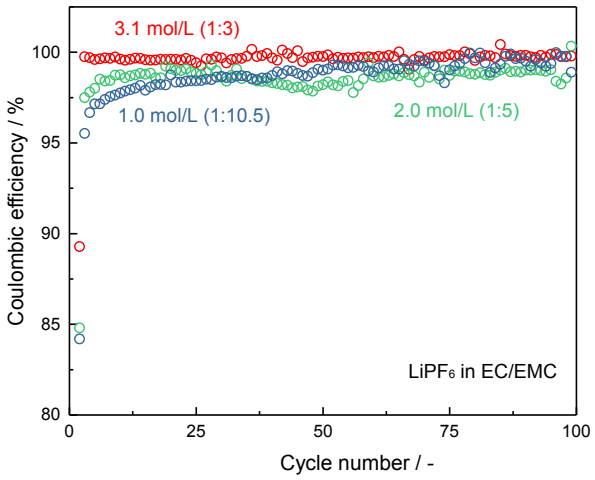

Figure S 9 Coulombic efficiency of battery cycling experiment on NMC811 composite electrode with different electrolyte concentration at room temperature. Original charge-discharge curves and capacity retention are shown in **Figure 2**. Coulombic efficiency of EIS cycle (1st and 100th cycle) are not plotted.

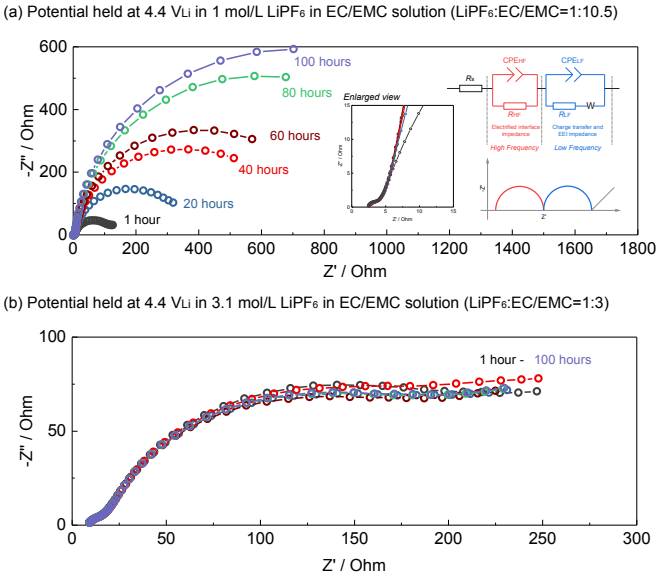

Figure S 10 Nyquist plots for EIS measurement on NMC811 composite electrode in NMC811|$Li_4Ti_5O_{12}$-mesh|Li three electrode cell with potential held at 4.4 V_{Li} in (a) 1.0 M and (b) 3.1 M $LiPF_6$ / EC-EMC (3:7 wt/wt) solution at 25 ºC. The cells were galvanostatically charged at 27.5 mA/g (0.1C) and held potential for 100 hours at 4.4 V_{Li}. Two semicircles were observed in the Nyquist plots for Li intercalation into composite electrodes like previous work.[2] The high-frequency semicircle (left) has been assigned to impedance at the electrified interface (predominantly lithium ion migration and adsorption/desorption in the pore structure of composite electrode) while the low-frequency semicircle (right) corresponds to the combination of charge transfer resistance at the electrode-electrolyte interface (equivalent circuit can be found in the inset).

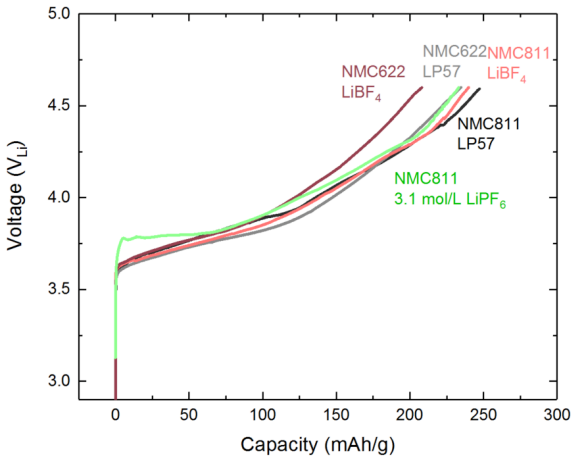

Figure S 11 Electrochemical profiles of $LiNi_{0.6}Mn_{0.2}Co_{0.2}O_2$ (NMC622) and $LiNi_{0.8}Mn_{0.1}Co_{0.1}O_2$ (NMC811) pellet electrodes charged to 4.6 V_{Li} at a 0.01C rate.

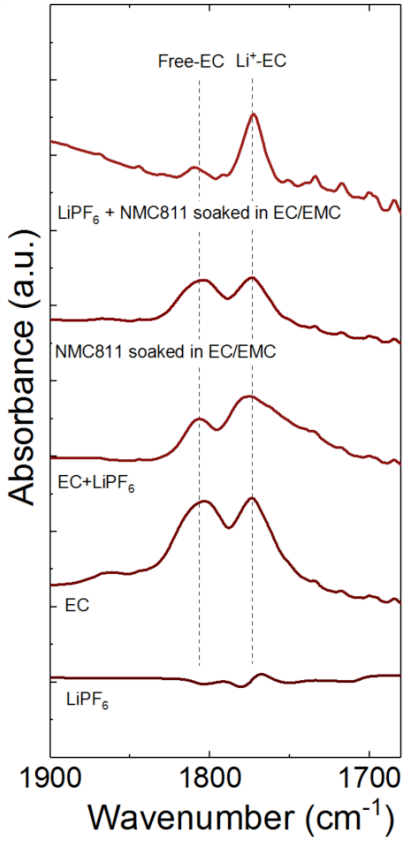

Figure S 12 DRIFT spectra of C=O stretching region for $LiPF_6$, EC, EC+$LiPF_6$ mixture, $Li_xNi_{0.8}Mn_{0.1}Co_{0.1}O_2$ (NMC811) soaked in EC:EMC (3:7wt) solution, $LiPF_6$ + soaked NMC811 in EC/EMC. Cumulative number of 256 was used at a 4 cm^{-1} resolution. Spectra were subtracted with respect to a reference spectrum obtained with potassium bromide (KBr) powder. Although Li^+-EC band and free EC band around 1770 cm^{-1} are overlapping,[3] peak intensity ratio change between free EC and Li^+-EC indicates meaningful difference for the amount of free EC and Li^+-EC in the DRIFT samples.

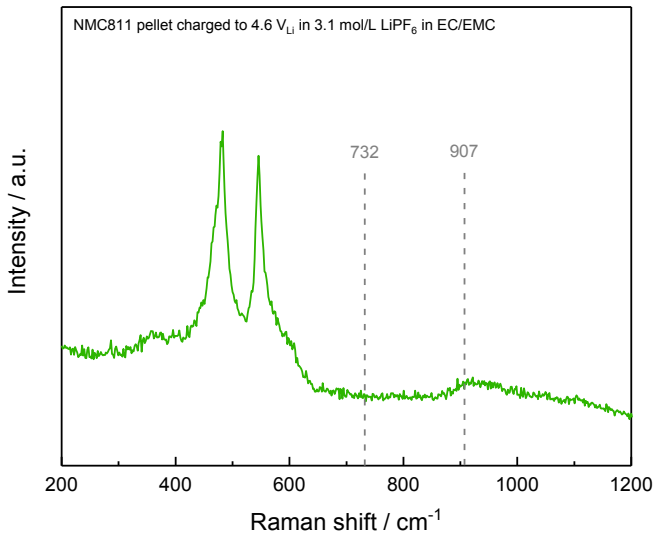

Figure S 13 Raman spectra for charged $Li_xNi_{0.8}Mn_{0.1}Co_{0.1}O_2$ (NMC811) to 4.6 V_{Li}, where peaks at ~732 and ~907 cm^{-1} is not emerged. The peaks at ~732 and ~907 cm^{-1} can be attributed to the ring distortion and the ring breathing mode of dehydrogenated Li^+-EC.

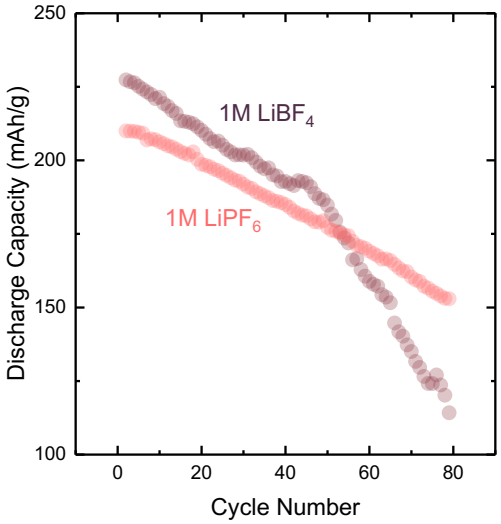

Figure S 14 Capacity retention as a function of cycles for NMC811 cycled between 4.6 V_{Li} and 2 V_{Li} in 1.0 M $LiPF_6$ in EC/EMC (3:7 w:w) and 1.0 M $LiBF_4$ in EC/EMC (3:7 w:w), with rate of 1 C (~275 mA/g) by using coin cell.

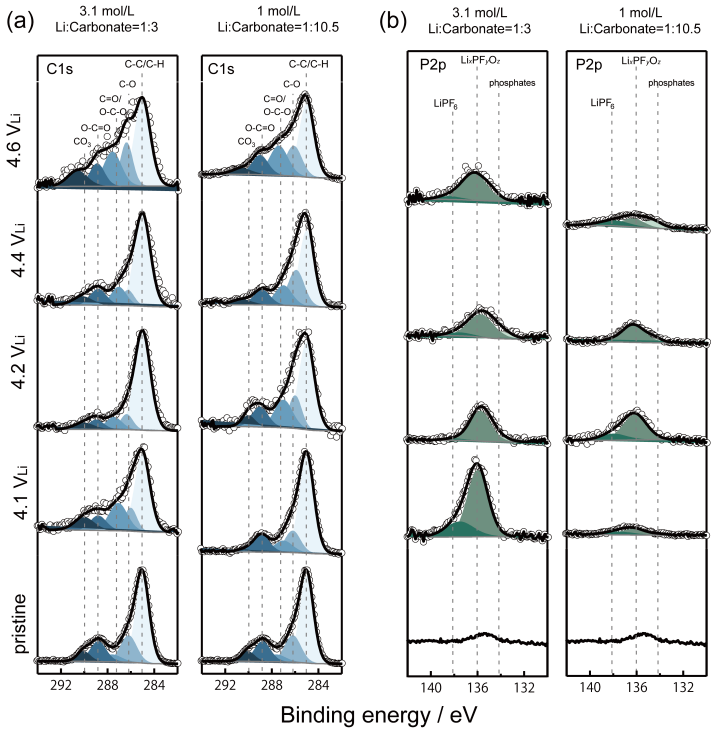

Figure S 15 Concentration dependent XPS spectra of the (a) C1s and (b) P2p photoemission lines collected from carbon-free, binder-free NMC811 electrodes (O1s and F1s spectra, and quantification results are shown in **Figure 5**). The electrodes were charged to 4.1, 4.2, 4.4 and 4.6 V_{Li} at 2.75 mA/g (0.01C) and held at the given potential for 5 hours using 1.0 M $LiPF_6$ in EC: EMC (3:7 wt:wt) and 3.1 M $LiPF_6$ in EC: EMC (3:7 wt:wt) solution and compared with pristine electrodes. All spectra were calibrated with the C1s photoemission peak of adventitious carbon at 285 eV. After subtraction of a Shirley-type background, all the spectra were normalized by fixing the C1s photoemission peak of adventitious carbon (285 eV) to the same value to facilitate comparison between samples. The spectra were assigned with the following contributions.[3] C1s: C-H/C-C (E_b = 285 eV), C-O (E_b~286.3 eV), C=O/O-C-O (E_b~287.6 eV), O=C-O (E_b~288.8 eV) and CO_3 (E_b~290.3 eV). P2p: phosphates (E_b~134 eV), $Li_xPF_yO_z$ (E_b~136 eV) and $LiPF_6$ (E_b~137.7 eV).

Table S 4 Binding Energies (eV) and Atomic Percentages (%) of the components from C1s, O1s, F1s, P2p, Li1s, Co2p, Mn2p, and Ni2p from the XPS Spectra of NMC 811 carbon-free, binder-free electrodes charged at different potentials using 3.1 M $LiPF_6$ in EC: EMC (3:7 wt:wt) as an electrolyte. 1.0 M data are available in previous publication. [3]

NMC811		Pristine			4.1V			4.2V			4.4V			4.6V		
Peak	Species	BE (eV)	FWHM (eV)	At%	BE (eV)	FWHM (eV)	At%	BE (eV)	FWHM (eV)	At%	BE (eV)	FWHM (eV)	At%	BE (eV)	FWHM (eV)	At%
C1s	C-C/C-H	285	1.4	20.63	285	1.5	6.9	285	1.6	21.5	285	1.6	13.8	285	1.6	7.3
	C-O	286.2	1.6	7.31	286.0	1.2	1.6	286.4	1.2	2.5	286.3	1.2	1.7	286.4	1.2	2.8
	C=O/O-C-O	287.6	1.8	2.17	287.1	1.8	2.9	287.5	1.6	2.6	287.0	1.5	2.6	287.6	1.8	3.2
	O=C-O	288.8	1.6	5.39	288.8	2.0	1.3	289.0	1.5	1.9	288.8	1.6	2.4	288.9	1.5	1.7
	CO3	290.0	1.3	2.21	290.0	1.3	1.5	290.0	2.0	1.7	290.1	2.0	1.6	290.6	2.0	1.7
O1s	O lattice	529.0	1.6	6.10	529.7	1.6	1.6	529.7	1.3	0.9	529.9	1.6	2.5	529.2	1.3	4.8
	ROLi	530.9	1.8	6.85	530.9	1.5	1.2	530.9	1.7	3.9	530.9	1.5	3.2	530.7	1.8	6.4
	Osurf/CO3/O-C=O	531.9	1.6	17.81	532.2	1.8	7.7	532.2	1.7	11.6	532.0	1.8	10.8	532.2	1.8	5.8
	C-O/O-C=O/OP(OR)3	533.6	1.5	2.22	533.4	1.7	4.3	533.4	1.4	4.1	533.4	1.6	3.7	533.4	1.4	2.7
	LixPFyOz	534.9	1.4	0.28	534.8	1.8	1.9	534.9	1.4	0.4	534.7	1.8	0.9	534.6	1.8	2.3
F1s	LiF	685.0	1.8	1.90	685.4	1.8	11.4	685.2	1.8	10.1	685.0	1.8	11.5	685.3	1.8	16.5
	LixPFyOz	687.0	1.8	0.24	687.0	1.8	15.1	686.5	2.0	5.4	686.5	2.0	10.3	686.5	1.8	7.5
	LiPF6	688.0	2.0	1.54	688.3	2.3	12.6	688.0	2.2	7.2	688.0	2.1	5.5	688.3	2.3	4.4
P2p	phosphate	133.9	2.5	0.11	/	/	/	134.8	2.5	0.7	134.3	2.5	0.6	134.8	1.5	0.2
	LixPFyOz	135.5	2.2	0.66	135.9	2.1	2.6	135.8	2.1	2.8	135.7	2.5	1.7	136.3	2.5	1.5
	LiPF6	138.1	0.5	0.02	137.5	2.8	0.8	138.1	2.3	0.2	137.5	2.4	0.2	138.5	2.3	0.1
Li1s	NMC/LiF	55.3	2.2	19.27	56.8	2.2	19.0	56.2	1.8	16.2	56.1	2.1	18.6	56.3	2.1	19.4
	LiPF6	/	/	/	/	/	/	/	/	/	/	/	/	/	/	/
Co2p	NMC	779.3	2.2	0.31	/	/	/	780.9	5.0	0.6	780.5	4.5	0.8	780.1	4.2	1.0
	satellite	/	/		/	/		/	/		/	/		/	/	
Ni2p	NMC	854.3	2.1	2.3	855.9	3.3	5.0	856.3	3.9	3.7	855.9	3.0	5.2	855.3	2.7	6.6
	satellite	861.1	4.4		861.1	7.1		862.5	4.5		859.9	4.3		858.9	4.1	
Mn2p	NMC	641.7	6.9	2.7	642.0	5.0	1.4	642.5	5.0	1.8	641.6	5.0	2.4	641.1	5.0	3.9

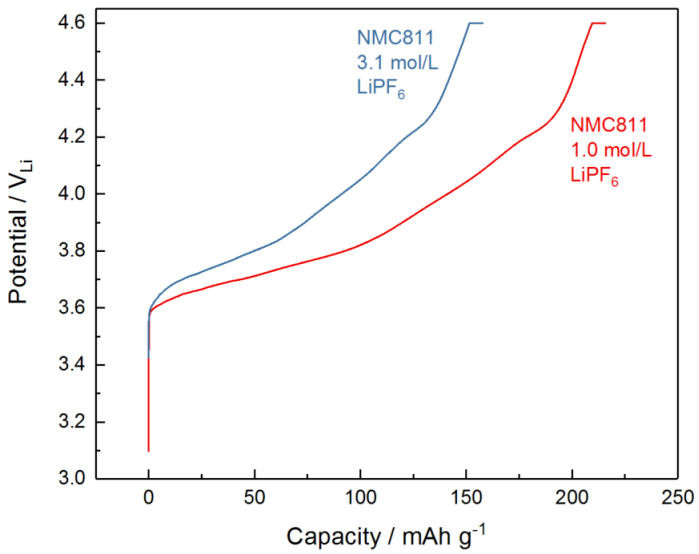

Figure S 16 Electrochemical profile of NMC811 carbon-free, binder-free electrodes charged at 100/C to 4.6 V_{Li} using 3.1 M and 1.0 M $LiPF_6$ in EC: EMC 3:7 (wt:wt). Overpotential for 3.1 M is most likely due to higher viscosity and lower ionic conductivity. Note that carbon-free, binder-free electrodes were prepared by just drop casting oxide powder on to Al foil and have poor contact.

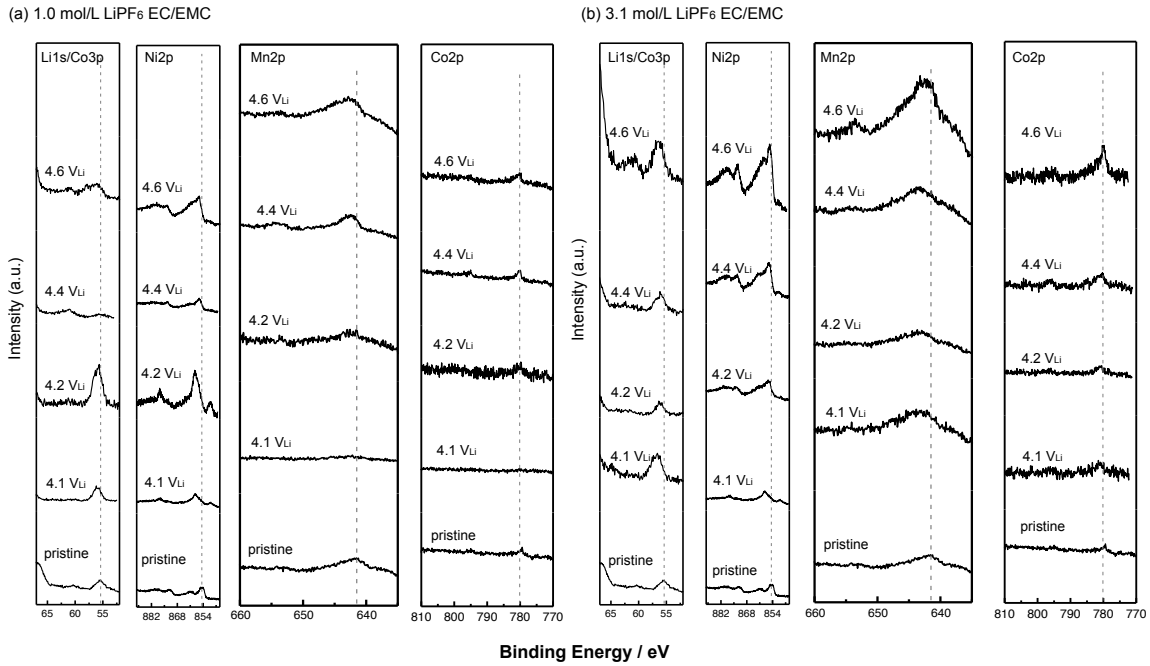

Figure S 17 Li1s/Co3p, Ni2p, Mn2p and Co2p XPS spectra of NMC811 carbon-free, binder-free pristine electrodes and after charging at 4.1, 4.2, 4.4, and 4.6 V_{Li} using (a) 1.0 M $LiPF_6$ and (b) 1.0 M in EC:EMC 3:7 (wt:wt).

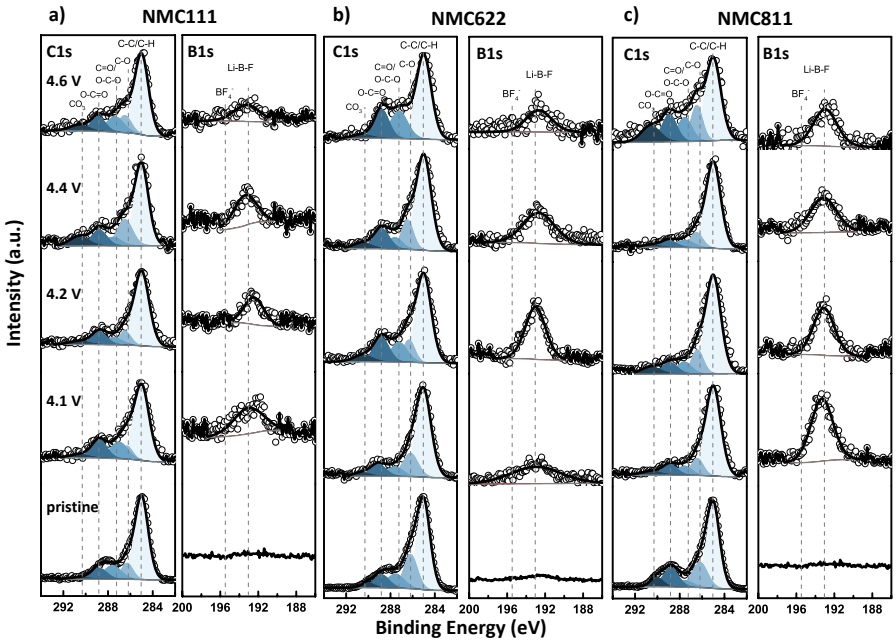

Figure S 18 C1s and B1s XPS spectra of (a) NMC111, (b) NMC622 and (c) NMC811 carbon-free, binder-free pristine electrodes and after charging at 4.1, 4.2, 4.4, and 4.6 V_{Li} using 1.0 M $LiBF_4$ in EC:EMC 3:7 (wt:wt).

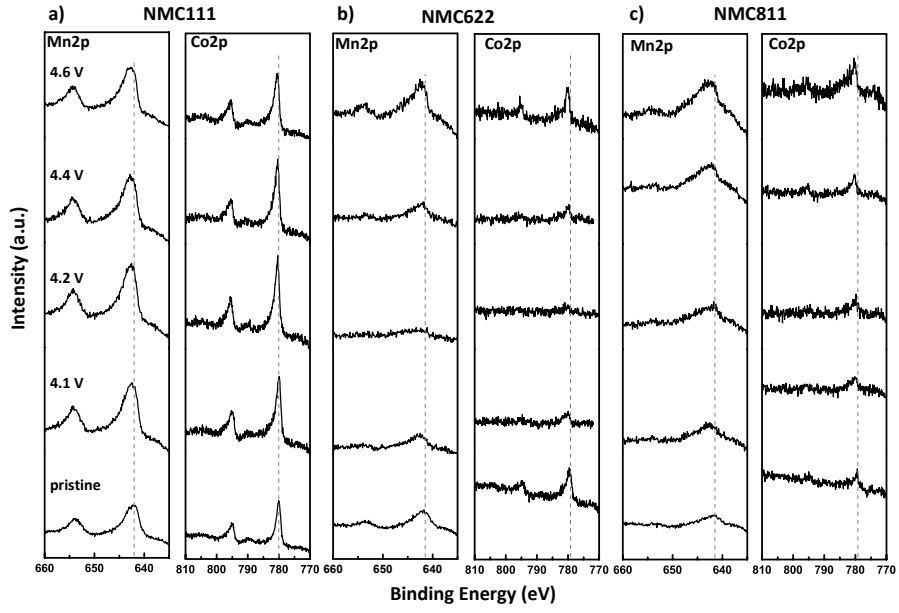

Figure S 19 Mn2p and Co2p XPS spectra of (a) NMC111, (b) NMC622 and (c) NMC811 carbon-free, binder-free pristine electrodes and after charging at 4.1, 4.2, 4.4, and 4.6 V_{Li} using 1.0 M $LiBF_4$ in EC:EMC 3:7 (wt:wt).

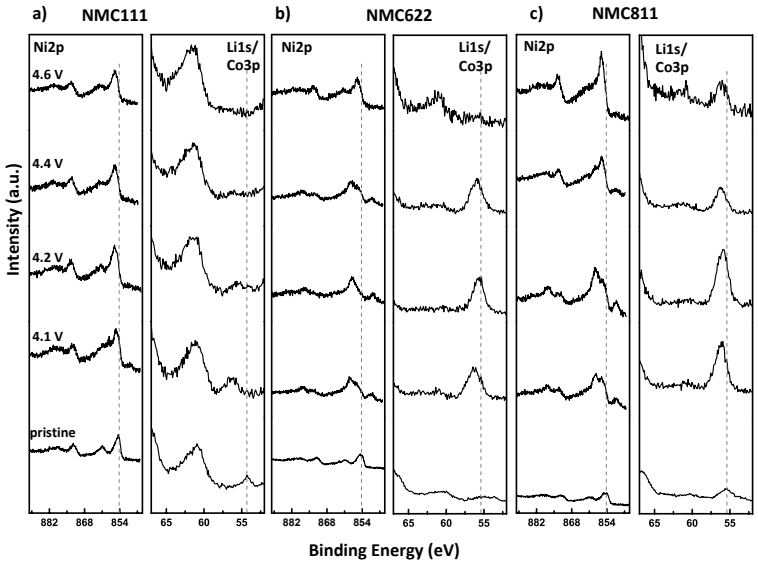

Figure S 20 Ni2p and Co3p/Li1s XPS spectra of (a) NMC111, (b) NMC622 and (c) NMC811 carbon-free, binder-free pristine electrodes and after charging at 4.1, 4.2, 4.4, and 4.6 V_{Li} using 1.0 M $LiBF_4$ in EC:EMC 3:7 (wt:wt).

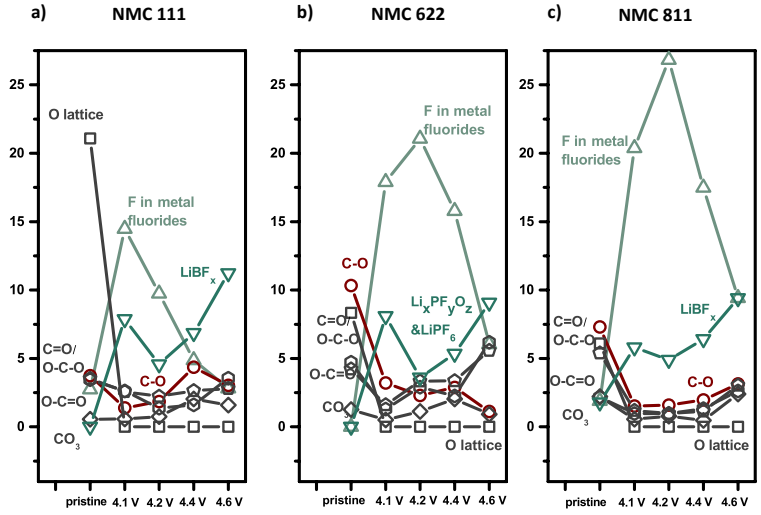

Figure S 21 Atomic percentages of XPS spectra for F in metal fluorides, C-O bonds, C=O/O-C-O, O-C=O and CO_3 bonds (from C1s in Figure S18), and O lattice in the pristine and charged (a) NMC111, (b) NMC622, (c) NMC811 carbon-free, binder-free electrodes at 4.1, 4.2, 4.4, and 4.6 V_{Li} using 1.0 M $LiBF_4$ in EC: EMC 3:7 (wt:wt).

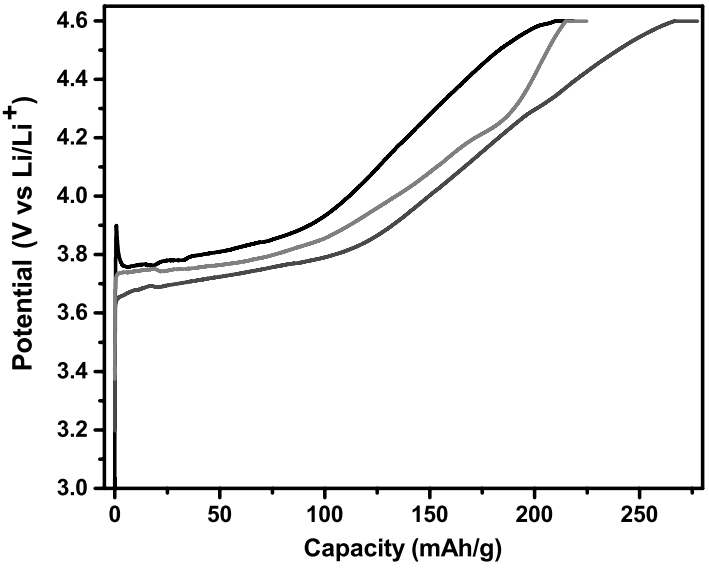

Figure S 22 Electrochemical profile of (a) NMC111 (black) (b) NMC622 (dark gray) (c) NMC811 (gray) carbon-free, binder-free pristine electrodes charged at 4.6 V_{Li} using 1.0 M $LiBF_4$ in EC: EMC 3:7 (wt:wt).

Table S 5 Binding Energies (eV) and Atomic Percentages (%) of the components from C1s, O1s, F1s, B1s, Li1s, Co2p, Mn2p, and Ni2p from the XPS Spectra of NMC111 carbon-free, binder-free electrodes charged at different potentials using 1.0 M $LiBF_4$ in EC: EMC (3:7 wt:wt) as an electrolyte.

NMC 111		Pristine			4.1V			4.2V			4.4V			4.6V		
Peak	Species	BE (eV)	FWHM (eV)	At%	BE (eV)	FWHM (eV)	At%	BE (eV)	FWHM (eV)	At%	BE (eV)	FWHM (eV)	At%	BE (eV)	FWHM (eV)	At%
C1s	C-C/C-H	285	1.5	21.5	285	1.6	10.7	285	1.6	13.0	285	1.5	12.5	285	1.5	15.6
	C-O	286.4	1.5	3.7	286.3	1.2	1.4	286.5	1.2	1.8	286.5	1.6	4.3	286.5	1.4	3.0
	C=O/O-C-O	287.6	1.7	3.5	287.0	1.8	2.6	287.5	1.8	1.4	287.6	1.8	1.6	287.4	1.8	3.5
	O=C-O	288.8	1.6	3.5	288.8	1.6	2.6	288.8	1.6	2.2	288.8	1.6	2.6	288.9	1.5	2.8
	CO3	290.6	1.7	0.6	290.6	2.0	0.6	290.6	2.0	0.8	290.6	2.0	2.0	290.6	2.0	1.6
O1s	O lattice	529.5	1.3	21.1	529.7	1.3	11.2	529.9	1.3	16.2	529.9	1.3	13.8	529.9	1.3	14.2
	ROLi	531.0	1.5	6.1	530.7	1.8	5.4	530.9	1.5	4.8	530.8	1.7	4.9	530.7	1.7	5.4
	Osurf/CO3/O-C=O	531.8	1.6	9.3	531.9	1.8	8.7	532.0	1.8	11.8	532.1	1.7	11.0	531.9	1.8	13.1
	C-O/O-C=O/OP(OR)3	533.4	1.7	2.0	533.4	1.8	3.9	533.4	1.7	3.4	533.7	1.8	6.8	533.4	1.8	5.6
	/	/	/	/	/	/	/	/	/	/	/	/	/	/	/	/
F1s	LiF	685.0	2.0	2.8	685.4	1.8	14.5	685.0	1.8	9.8	685.3	1.6	4.9	685.0	1.8	2.2
	LixBFy	686.6	1.8	0.9	686.5	2.2	5.4	686.5	1.8	3.7	686.6	2.3	5.4	686.5	2.2	5.6
	LiBF4	688.5	2.3	1.5	688.5	2.3	1.3	688.5	1.8	0.9	688.5	2.3	1.5	688.5	2.3	6.5
B1s	LixBFy	/	/	/	193.0	3.7	4.8	192.4	2.4	4.1	193.4	2.8	5.6	193.1	3.2	4.1
	LiBF4	/	/	/	/	/	/	/	/	/	/	/	/	/	/	/
Li1s	NMC	54.4	1.3	11.3	/	/	/	/	/	/	/	/	/	/	/	/
	Li2CO3/LiF	/	/	/	56.4	2.0	15.0	55.7	2.4	12.5	56.3	2.3	7.7	/	/	/
Co2p	NMC	779.9	1.3	2.5	779.9	1.7	2.7	780.4	1.5	2.4	780.5	1.6	2.9	780.6	1.7	3.1
	satellite	789.7	3.0		789.5	8.0		/	/		789.9	3.0		789.6	3.0	
Ni2p	NMC	854.6	1.8	4.3	855.1	2.5	4.7	855.7	2.5	5.3	855.7	3.0	5.7	855.6	2.3	5.5
	satellite	861.2	4.0		860.7	6.0		862.3	4.8		862.2	6.0		862.3	6.0	
Mn2p	NCM	641.9	2.3	4.4	642.3	2.5	3.9	642.5	2.5	5.3	642.6	2.5	4.7	642.5	2.4	5.1

Table S 6 Binding Energies (eV) and Atomic Percentages (%) of the components from C1s, O1s, F1s, B1s, Li1s, Co2p, Mn2p, and Ni2p from the XPS Spectra of NMC622 carbon-free, binder-free electrodes charged at different potentials using 1.0 M $LiBF_4$ in EC: EMC (3:7 wt:wt) as an electrolyte.

NMC622		Pristine			4.1V			4.2V			4.4V			4.6V		
Peak	Species	BE (eV)	FWHM (eV)	At%	BE (eV)	FWHM (eV)	At%	BE (eV)	FWHM (eV)	At%	BE (eV)	FWHM (eV)	At%	BE (eV)	FWHM (eV)	At%
C1s	C-C/C-H	285	1.4	24.42	285	1.6	11.5	285	1.6	12.1	285	1.6	11.3	285	1.6	16.9
	C-O	286.2	1.5	10.33	286.2	1.6	3.2	286.3	1.2	2.3	286.5	1.2	2.7	286.5	1.2	1.1
	C=O/O-C-O	287.6	1.8	4.72	287.6	1.7	1.3	287.2	1.7	2.9	287.6	1.5	1.3	287.2	1.8	6.2
	O=C-O	288.8	1.6	4.23	289.1	1.6	1.6	288.8	1.6	3.3	288.8	1.6	2.4	288.8	1.5	5.9
	CO3	290.0	1.3	1.26	290.6	1.7	0.5	290.5	2.0	1.1	290.3	2.0	0.8	290.6	2.0	0.9
O1s	O lattice	528.9	1.5	8.33	529.6	1.3	1.6	529.4	1.3	0.9	529.3	1.3	1.5	529.4	1.3	8.5
	ROLi	530.8	1.8	6.21	530.9	1.8	1.6	530.8	1.6	1.1	530.6	1.8	1.6	530.9	1.6	6.7
	Osurf/CO3/O-C=O	531.9	1.8	14.37	532.2	1.7	11.7	532.2	1.8	11.7	531.9	1.8	16.5	532.1	1.7	11.4
	C-O/O-C=O/OP(OR)3	533.5	1.6	3.12	533.4	1.8	2.9	533.6	1.8	3.9	533.4	1.8	4.0	533.9	1.8	6.7
	/	/	/	/	/	/	/	/	/	/	/	/	/	/	/	/
F1s	LiF	/	/	/	685.5	1.8	17.9	685.0	1.8	20.9	685.3	1.8	16.7	685.0	1.8	6.7
	LixBFy	/	/	/	686.5	1.8	6.2	687.0	1.8	2.7	686.5	1.8	3.7	687.0	2.3	6.0
	LiBF4	/	/	/	688.5	2.3	1.9	688.5	2.3	3.9	688.4	1.8	0.5	688.5	3.4	3.7
B1s	LixBFy	/	/	/	193.0	6.3	5.1	193.0	2.5	6.3	192.7	3.9	5.0	192.7	3.2	5.1
	LiBF4	/	/	/	/	/	/	/	/	/	/	/	/	/	/	/
Li1s	NMC	54.9	3.2	15.64	/	/	/	/	/	/	/	/	/	/	/	/
	Li2CO3/LiF	/	/	/	56.2	2.1	28.5	55.6	1.8	27.6	56.0	2.2	28.2	56.1	2.2	5.8
Co2p	NMC	779.5	1.8	0.85	780.2	2.9	2.0	/	/	/	780.0	2.4	1.2	780.1	1.9	2.2
	satellite	789.2	4.0		/	/		/	/		/	/		/	/	
Ni2p	NMC	854.3	2.0	2.98	857.0	4.7	2.2	857.3	3.0	1.8	857.0	3.0	2.2	855.6	2.9	4.1
	satellite	861.3	4.4		859.0	1.5		/	/		/	/		/	/	
Mn2p	NCM	642.0	4.8	3.04	642.4	4.2	0.9	642.2	5.0	0.8	641.6	4.6	1.0	642.2	3.4	3.0

Table S 7 Binding Energies (eV) and Atomic Percentages (%) of the components from C1s, O1s, F1s, B1s, Li1s, Co2p, Mn2p, and Ni2p from the XPS Spectra of NMC811 carbon-free, binder-free electrodes charged at different potentials using 1.0 M $LiBF_4$ in EC: EMC (3:7 wt:wt) as an electrolyte.

NMC 811		Pristine			4.1V			4.2V			4.4V			4.6V		
Peak	Species	BE (eV)	FWHM (eV)	At%	BE (eV)	FWHM (eV)	At%	BE (eV)	FWHM (eV)	At%	BE (eV)	FWHM (eV)	At%	BE (eV)	FWHM (eV)	At %
C1s	C-C/C-H	285	1.4	20.63	285	1.6	10.4	285	1.6	8.4	285	1.6	14.1	285	1.6	9.2
	C-O	286.2	1.6	7.31	286.4	1.2	1.5	286.4	1.2	1.6	286.5	1.3	2.0	286.5	1.2	3.0
	C=O/O-C-O	287.6	1.8	2.17	287.6	1.5	1.0	287.6	1.5	1.0	287.5	1.8	1.3	287.6	1.5	2.5
	O=C-O	288.8	1.6	5.39	288.9	1.6	1.2	288.9	1.6	1.0	289.0	1.6	1.1	288.9	1.5	2.9
	CO3	290.0	1.3	2.21	290.6	2.0	0.6	290.6	2.0	0.8	290.6	1.7	0.5	290.6	2.0	2.3
O1s	O lattice	529.0	1.6	6.10	529.4	1.3	1.6	529.1	1.3	0.3	529.5	1.3	4.2	529.6	1.3	7.4
	ROLi	530.9	1.8	6.85	530.5	1.5	2.4	530.6	1.6	2.6	530.8	1.5	4.0	530.9	1.5	5.8
	Osurf/CO3/O-C=O	531.9	1.6	17.81	532.2	1.8	7.2	532.2	1.8	5.8	532.2	1.8	7.2	532.2	1.8	12.0
	C-O/O-C=O/OP(OR)3	533.6	1.5	2.22	533.4	1.8	4.7	533.4	1.7	2.8	533.4	1.8	4.4	533.9	1.8	6.4
	/	/	/	/	/	/	/	/	/	/	/	/	/	/	/	/
F1s	LiF	685.0	1.8	1.90	685.4	1.7	20.4	685.1	1.7	26.8	685.4	1.7	17.5	685.4	1.8	8.9
	LixBFy	687.0	1.8	0.24	686.5	1.8	2.5	686.5	2.0	4.2	686.5	2.1	3.7	686.6	2.1	4.4
	LiBF4	688.0	2.0	1.54	688.4	2.3	3.3	688.2	2.3	0.8	688.4	2.3	2.4	688.5	2.3	4.6
B1s	LixBFy	/	/	/	193.3	2.7	6.9	193.1	2.6	4.1	193.1	3.3	6.6	193.0	2.9	4.9
	LiBF4	/	/	/	/	/	/	/	/	/	/	/	/	/	/	/
Li1s	NMC	55.3	2.2	19.27	/	/	/	/	/	/	/	/	/	/	/	/
	Li2CO3/LiF	/	/	/	56.2	1.8	31.0	56.0	1.8	32.5	56.2	1.7	22.4	56.1	1.8	14.4
Co2p	NMC	779.3	2.2	0.31	780.3	2.9	0.3	780.2	3.8	0.4	780.2	2.9	0.8	780.7	3.5	1.3
	satellite	/	/		/	/		/	/		789.5	4.9		789.5	5.8	
Ni2p	NMC	854.3	2.1	2.3	855.9	3.0	3.3	857.7	6.2	4.3	855.7	2.7	5.1	855.9	2.6	3.9
	satellite	861.1	4.4		859.5	6.0		/	/		858.7	4.7		862.6	6.0	
Mn2p	NCM	641.7	6.9	2.7	641.6	5.0	3.3	641.7	4.6	1.1	641.8	4.6	2.4	641.7	4.4	1.0

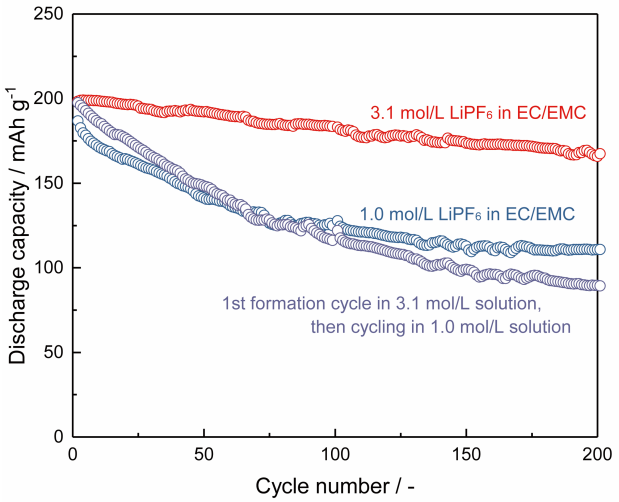

Figure S 23 Cycling performance of NMC811 composite electrodes upon charging to 4.6 V_{Li} (2nd-99th cycle at CC-CV 1C-0.05C condition). The electrode cycled in 3.1 M $LiPF_6$ in EC/EMC solution for 1st cycle, replaced electrolyte to 1.0 M solution and started 2nd cycle. At the 1st and 100th cycle, the cells were measured in a three-electrode configuration, which composed of NMC811|$Li_4Ti_5O_{12}$-mesh|Li (see experimental section in detail), galvanostatically charged at 27.5 mA/g (0.1C). From the 2nd to the 99th cycle and after 101st cycle, the cells were tested with a two-electrode configuration that consisted NMC811 as the working electrode and Li metal as the counter electrode. The collected electrode was washed with 1.0 M solution before cell assembly.

Table S 8 Calculated interaction energy between carbonyl oxygen of EC and the metal site of oxide surface (electrophilic attack), for $LiMO_2$ (M = Mn, Co and Ni) and $LiNiO_2$ where one surface Ni has been replaced with Co and Mn (Co-doped and Mn-doped $LiNiO_2$, respectively). The interaction energy of EC with Li^+ ion and $Li^+(EC)_n$ complexes (ion-dipole interaction), computed as the energy of the reaction: $Li^+(EC)_{n-1} + EC \rightarrow Li^+(EC)_n$, is also reported.

	Site	Interaction Energy / eV
$LiMnO_2$	Mn	-0.19
$LiCoO_2$	Co	-0.33
$LiNiO_2$	Ni	-0.50
$LiNiO_2$	Li	-0.41
Co-doped $LiNiO_2$	Co	-0.14
Mn-doped $LiNiO_2$	Mn	-0.26
$Li^+(EC)$	-	-2.37
$Li^+(EC)_2$	-	-1.19
$Li^+(EC)_3$	-	-0.78

Reference for Supporting Information

1. K. M. Diederichsen, H. G. Buss, and B. D. McCloskey, *Macromolecules,* **50**, 3831-3840 (2017).
2. R. Tatara, P. Karayaylali, Y. Yu, Y. Zhang, L. Giordano, F. Maglia, R. Jung, J. P. Schmidt, I. Lund, Y. Shao-Horn, *J. Electrochem. Soc.*, 166, A5090−A5098 (2019).
3. Y. Yu, P. Karayaylali, Y. Katayama, L. Giordano, M. Gauthier, F. Maglia, R. Jung, I. Lund, Y. Shao-Horn, *J. Phys. Chem. C,* **122**, 27368−27382 (2018).